5-18-2020

Geminate Triplet Exciton Dynamics in Rubrene Single Crystals

Eric Wolf
Lehigh University

Geminate Triplet Exciton Dynamics in Rubrene Single Crystals

Eric Wolf

May 6, 2020

1 Introduction

The core motivation of physics research is a desire to understand the behavior of the universe at a fundamental level. With that said, however, certain aspects of this behavior attract particular interest because of their practical implications. Consider, for instance, the following well-known result, derived by Shockley and Quiesser: a conventional, single bandgap solar cell operating at room temperature can achieve an efficiency of at most $\sim 30\%$.[1]

In one sense, this result is uninteresting, being nothing more than a consequence of the particularities of our sun's spectrum, geometrical factors, the nature of recombination in semiconductors, etc. In another sense, it is quite important. While solar energy still lags behind wind for non-hydroelectric renewable energy generation — in 2018, its share in this category was approximately 20% in the US, as compared to 50% for wind — it is growing rapidly, being responsible for about 50% of the growth in this area worldwide.[2] This rigorous, theoretically-derived limit for the efficiency of a photovoltaic solar cell, given its usefulness in informing R&D efforts, calculating capacities, etc., then becomes significant as a guide for solar energy generation efforts.

In their publication, however, Shockley and Quiesser note that they disregard a potential mechanism for efficiency increases beyond the theoretical limit. In particular, their "ultimate efficiency hypothesis" posits that any photon incident on a cell with an energy greater than the cell's bandgap E_g will produce a single charge carrier with an energy equal to that of the bandgap. They note, however, that it is in principle possible for photons with energies greater than $2E_g$ to produce multiple charge carriers, each at the bandgap energy. Calculations

suggest that, under ideal conditions, such carrier multiplication processes could increase the theoretical efficiency limit to $\sim 45\%$, well above the limit without multiplication.[3]

One avenue for realizing carrier multiplication is a process known as singlet fission (SF). In semiconductors, an electron which is excited to the conduction band may become bound through Coulomb attraction to the hole it leaves behind, and the resulting electron-hole pair is called an exciton. Through singlet fission, a photoexcited singlet (spin $S = 0$) exciton can split into two triplet ($S = 1$) excitons. Understanding the dynamics of the singlet fission process is crucial if it is to be used as a route to carrier multiplication.

Because of its high singlet fission efficiency, rubrene (5,6,11,12-tetraphenyltetracene) can be used as a model system in which to study this process. Additionally, near-degeneracy between the singlet and triplet pair energies in rubrene allows the reverse process to SF, namely fusion of triplet excitons and emission of a photon via radiative relaxation of the generated singlet state, to occur. The full singlet fission process in rubrene spans at least 6 time decades, with various references claiming timescales of $\sim$ 400 fs [4] to $\sim$ 10 ps [5] for initial triplet pair production from the first excited singlet state and with the ultimate exponential decay of isolated triplets occurring after $\sim 100\ \mu s$.[6] Within these dynamics, intermediate timescale processes (~ 1 ns $- 1\mu$ s) which depend sensitively on the evolution of the spatial and spin relationships between the SF-produced triplet pair have attracted less attention, despite the important information about triplet pair evolution that the study of these processes can offer.

In this work, we focus on the geminate triplet pair, where "geminate" denotes triplets produced by the same singlet fission event. We present a series of investigations on the intermediate timescale dynamics of geminate triplet exciton pairs in rubrene single crystals. In particular, we report the observation of quantum beats — GHz-timescale oscillations produced by energy splittings — in the photoluminescence of rubrene crystals [7], indicating coherence between triplet pairs which lasts at least 40 ns at room temperature. Additionally, we present long-timescale (up to 10 μ s) measurements of the PL dynamics of rubrene without a contribution from nongeminate triplet fusion; these measurements provide support for a random walk model of triplet diffusion and demonstrate a transition in this diffusion's dimensionality on a timescale of $\tau \sim 2\mu$s.

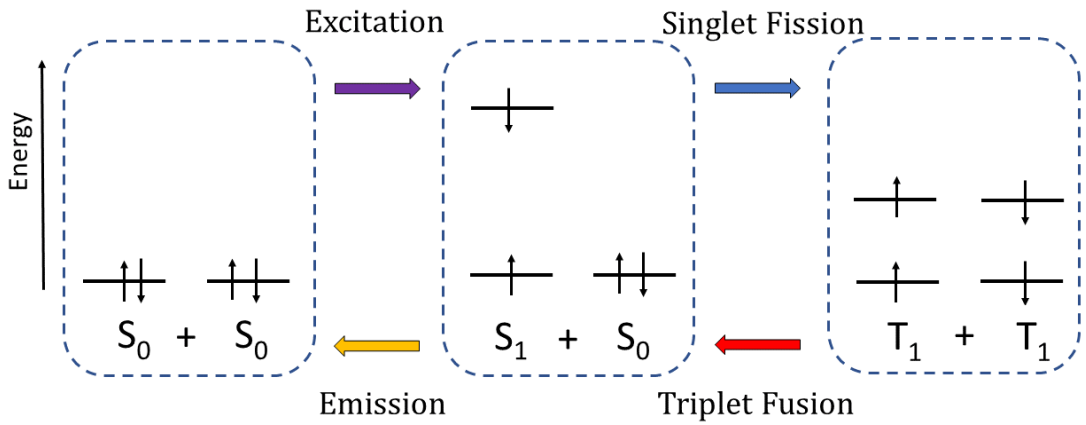

Figure 1: A schematic representation of the singlet fission and triplet fusion processes, along with photoexcitation and emission, in a typical organic semiconductor.

2 Basic Concepts

2.1 Singlet Fission

In Figure 1, we present a pictorial representation of the singlet fission process. In particular, for organic semiconductors like rubrene, the excitons involved in singlet fission may be thought of as Frenkel-type, i.e. being localized to a single lattice site and understood as a molecular excited state.[8, 9] Beginning at the left side of the figure, we imagine two adjacent rubrene molecules in the ground state, with two electrons occupying the Highest Occupied Molecular Orbital (HOMO). Note that, because electrons are fermions, their overall wavefunction must be antisymmetric under particle exchange; because the ground state spatial wavefunction is symmetric, the overall spin wavefunction of the ground state electron pair is an antisymmetric singlet $|0\ 0\rangle = \frac{1}{\sqrt{2}}\left(|\uparrow\rangle|\downarrow\rangle - |\downarrow\rangle|\uparrow\rangle\right)$. Upon absorption of a photon, one of the molecules may be excited to a higher (electronic) state S_1; given that the incoming photon does not couple to the spin degree of freedom of the electron in the electric dipole approximation, the resulting excited state will be a singlet as well.

At this point, it is possible for a molecular excited state S_1 to undergo singlet fission (SF) into a pair of triplet excitons on adjacent molecular sites. Informally, we may imagine this as

being accomplished by an "electron exchange" between adjacent molecules, with the spin-up electron from the excited molecule being exchanged with the spin-down electron from an adjacent one. More formally, we note that it is possible to construct a state with overall singlet character as a coherent superposition of triplet pair states. Using a Clebsch-Gordon table, we can write such a state in a basis of eigenstates of S_z as

$$|00\rangle = \frac{1}{\sqrt{3}} \left(|1\rangle |-1\rangle - |0\rangle |0\rangle + |-1\rangle |1\rangle \right)$$

From this, we see that singlet fission is a *spin*-allowed process. To understand how such a process can be energy conserving, we recall that the symmetry of the triplet spin wavefunction forces the spatial electron wavefunctions to be antisymmetric, which increases separation between electrons and reduces their Coulomb energy. In large organic molecules, it is possible for this energy shift to be sufficiently large that the energy E_S of the first excited singlet state is more than twice the energy E_T of the first excited triplet state. If this relation holds, then singlet fission is also an energy-allowed process.

It is possible in materials where the singlet-triplet energy difference is just right for the stronger condition $E_S \approx 2E_T$ to hold. If this is the case, then both singlet fission and a reverse process, triplet fusion (TF), may be energy-allowed (possibly after thermal activation in one of the two directions).

In the triplet fusion process, two triplet excitons recombine in order to re-form a singlet exciton. We expect (see e.g. [10]) that the probability of this process will be proportional to the overall singlet character of the pair of triplet excitons, i.e. to the overlap integral $|\langle 00|\Psi\rangle|^2$, where $|\Psi\rangle$ is the spin state of the triplet pair. Additionally, we expect that the fusion probability will depend on the overlap of the spatial wavefunctions of the triplet pair states. Triplet fusion may occur either between a pair of geminate triplets — geminate triplet fusion — or between triplets which are not members of a geminate pair — nongeminate triplet fusion.

In general, triplet fusion is an undesirable property in applications which seek to harness singlet fission for the purpose of carrier multiplication in solar cells: if triplet states are capable of fusing back into a singlet, triplet fusion and photoemission from the resulting singlet state constitutes a loss channel. However, triplet fusion is extremely useful as an experimental probe. In particular, recall the fact that a lone triplet exciton has spin 1, which implies that photoemission from a triplet state is an electric dipole-forbidden process.

Triplet excitons are thus "dark states" which do not photoluminesce. Accordingly, many experiments which investigate triplet dynamics have used pump-and-probe techniques like induced absorption spectroscopy.[11, 12, 5] However, as discovered by early investigators [13], triplet fusion provides a pathway by which these "dark" states can recombine and emit detectable photoluminescence. Additionally, because the fusion rate between triplets will, as we have discussed, depend on both the spatial and spin relationship between them, the dynamics of the triplet fusion-produced photoluminescence will encode information about these relationships.

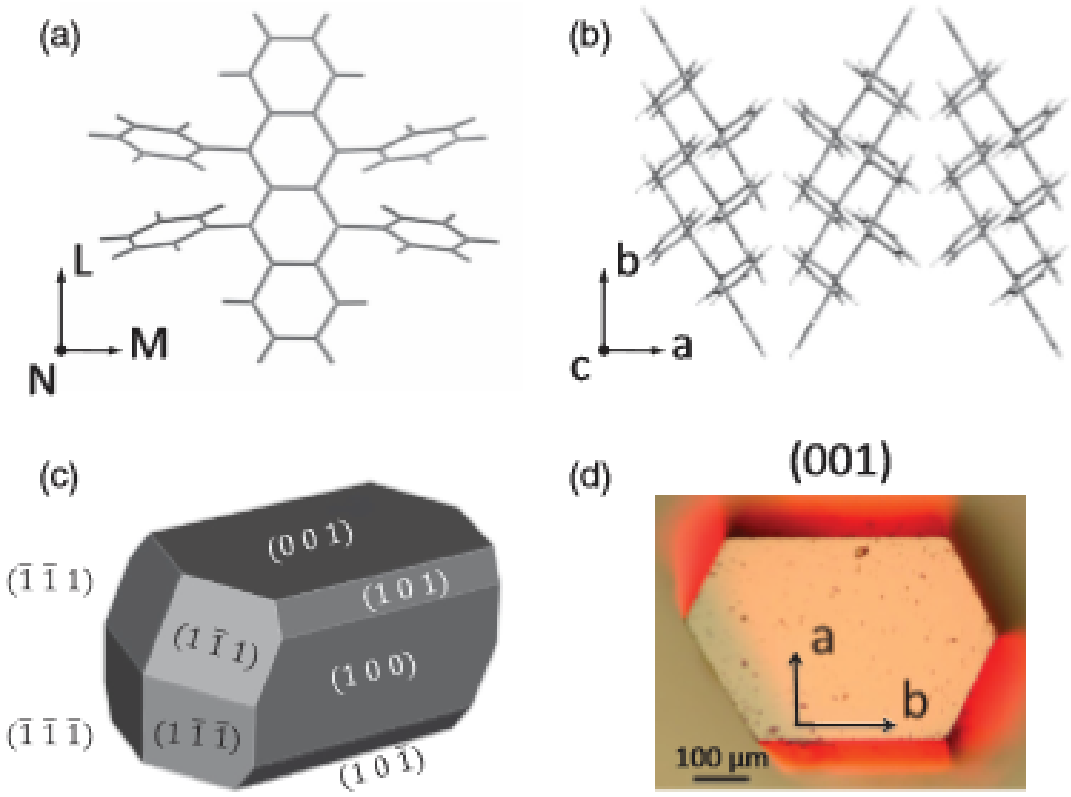

Figure 2: A figure depicting orthorhombic crystalline rubrene, our experimental system. a) represents a rubrene molecule, b) illustrates the typical "herringbone" stacking of rubrene molecules within the *ab*-plane, c) represents the simulated geometry of a small rubrene crystal, and d) is an image of a micrometer-sized "stubby" rubrene crystal. Figure taken from [14].

2.2 Rubrene

In Figure 2, we show several depictions of our experimental system, the organic semiconductor rubrene (5, 6, 11, 12-tetraphenyltetracene) in its orthorhombic crystalline form. Rubrene has a number of desirable properties for an experimental SF system; one such property is the near degeneracy between E_S and $2E_T$, as referenced above. In particular, the energy of the lowest excited triplet state in rubrene has been measured to be 1.14 ± 0.02 eV.[15] Likewise, a PL emission band at 2.22 eV, the highest in a vibrational series [14], gives a rough idea of the energy of the first excited singlet state. In light of this near degeneracy, it is unsurprising that enhancements in the photoluminescence of crystalline rubrene have been observed at relatively low CW illumination intensities, demonstrating highly efficient singlet fission and

triplet fusion in this system.[16]

Rubrene exhibits several additional properties which are relevant to studies of the dynamics of geminate singlet fission-produced triplets. For example, the isolated triplet lifetime in rubrene - i.e. the time constant for the exponential decay of triplet excitons which do not undergo triplet fusion - is approximately $100\mu s$.[6] This long lifetime allows the dynamics to be followed for tens of microseconds before exponential decay of triplets reduces the available photoluminescence signal, but it also implies that any photoluminescence experiments performed under CW or high repetition rate pulsed illumination will take place in the presence of a "sea" of long-lived triplets produced by previous excitation events. Likewise, the long diffusion length of triplet excitons along the crystalline b-axis of orthorhombic rubrene [17] makes it easier to observe the spatial diffusion of triplets but also implies that triplet excitons can travel long distances in order to encounter other, nongeminate triplets and produce photoluminescence that obscures the geminate photoluminescence signal.

Before proceeding, we make a few remarks about the photoluminescence spectra of rubrene single crystals. The first is that the photoluminescence spectrum of rubrene is highly polarization-dependent, as discussed in great detail in [14]. In particular, photoluminescence collected with a polarization within the plane normal to the crystalline c-axis has its first spectral peak at approximately 610 nm, whereas c-polarized light is emitted with much greater intensities (for identical excitation intensities) and has its first peak at approximately 560 nm. This difference is straightforward to explain. The $S_1 \rightarrow S_0$ transition dipole moment in rubrene is oriented along the molecular M-axis, as depicted in Figure 2; in turn, orthorhombic rubrene has all of the molecular M-axes oriented along the crystalline c-axis. Accordingly, photon emission from the $S_1 \rightarrow S_0$ transition is only dipole-allowed for c-polarized light, and so c-polarized photoluminescence is much brighter than ab-polarized photoluminescence. The apparent redshift of the highest-energy peak in the spectrum of ab-polarized light occurs because this light is emitted via a dipole-allowed transition from S_1 to a vibrationally excited ground state S_0'; an (electronic) ground state which is in a vibrationally excited state with the proper symmetry can have a nonzero transition dipole moment with the excited state S_1 within the ab plane.

Additionally, also as discussed in [14], crystalline rubrene samples occasionally exhibit a strong, atypical photoluminescence peak near 650 nm. An example of this atypical photoluminescence, along with a typical spectrum, is given in Figure 3. This photoluminescence peak has been observed by several different workers (e.g. [18, 19]) and has been attributed

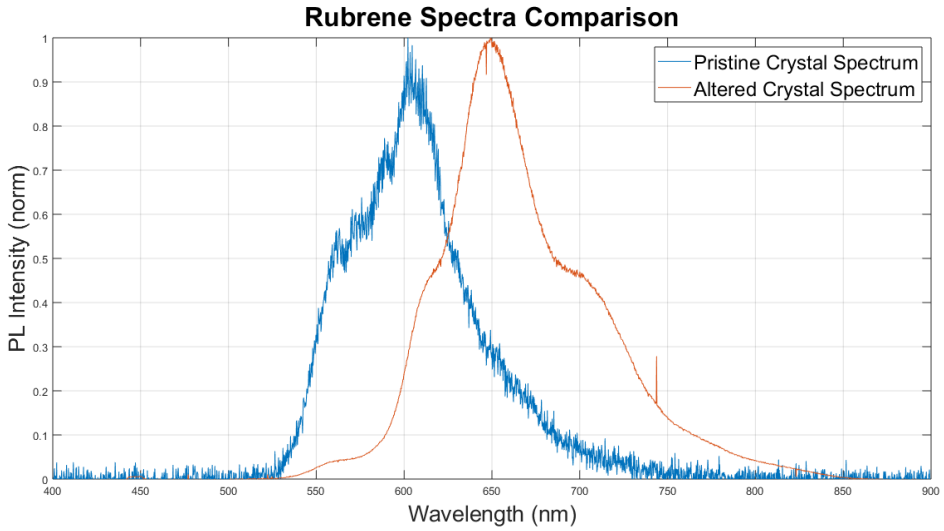

Figure 3: A comparison plot of normalized spectra for a "pristine" and "altered" crystal, with excitation and detection light polarized in the *ab* plane. The peak for the pristine spectrum occurs at approximately 610 nm, while that of the altered spectrum occurs at approximately 650 nm. Note that the small "spikes" on the altered crystal are unphysical and likely corresponds to pixel errors on the spectrometer.

by some to oxidation. [20, 21] Irrespective of the origin of this PL signature, we find that the photoluminescence dynamics associated with this particular spectral feature differ from those of "pristine" rubrene, a fact which we will treat in more detail later. Consequently, we generally restrict our observations to "pristine" rubrene crystals in which this 650 nm emission band is not as prominent.

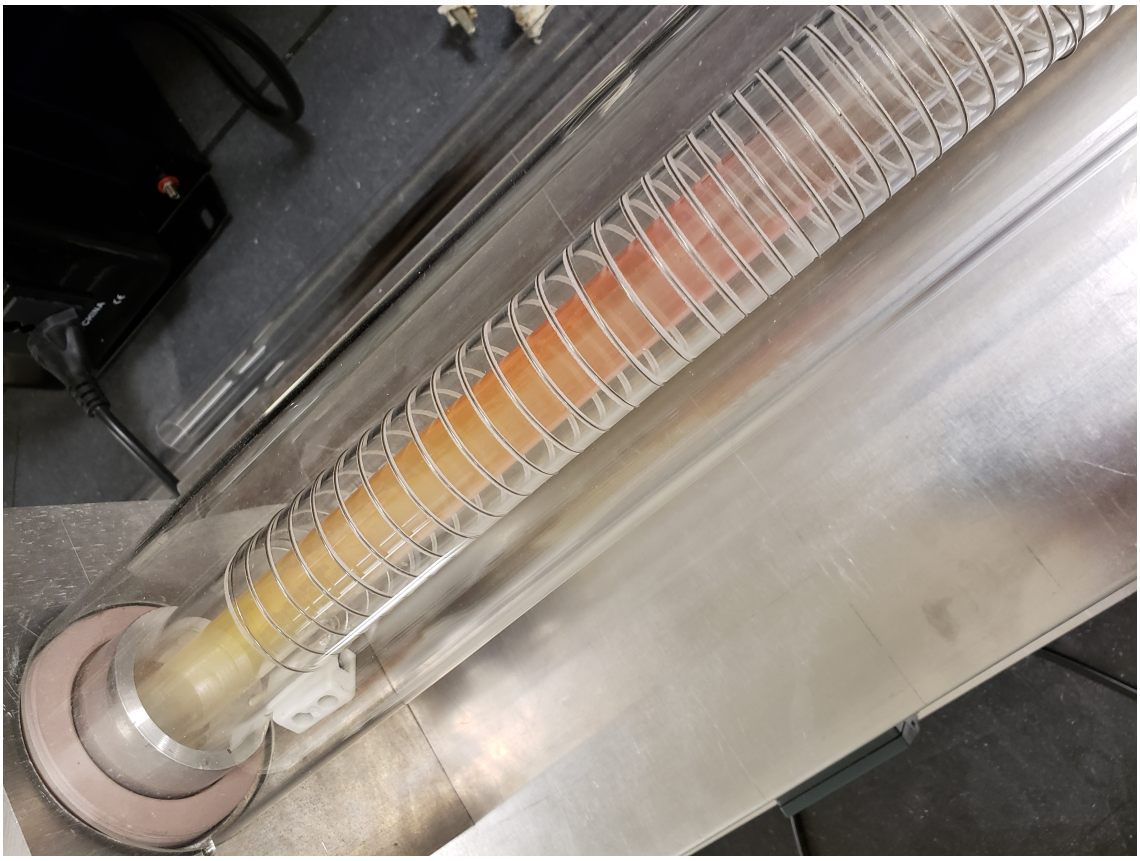

Figure 4: A photo of the physical vapor transport setup during crystal growth, seen from above.

3 Experimental Methods

3.1 Sample Preparation

We prepare rubrene single crystals from 99% pure ACROS Organics rubrene powder using a physical vapor transport technique;[22] the experimental setup is depicted in Figure 4. Argon gas is used in order to prevent oxidation of the growing crystals, as remarked upon above. Typical flow rates are $\approx 50\ \frac{\text{mL}}{\text{min}}$ in a tube with a diameter of 1 in. We conduct our measurements on "platelet" single crystals with mm-scale extensions along the crystalline a and b axes and thicknesses (along the c-axis) of $\sim 100\ \mu$m, as depicted in Figure 5. These crystals are subsequently mounted on glass slides using commercially available Scotch black electrical tape (chosen for its relative lack of photoluminescence under laser excitation) and stored in dark containers, exposed to ambient air. We have not observed any long-term changes in the spectra or PL dynamics of crystals stored in this way, even after several

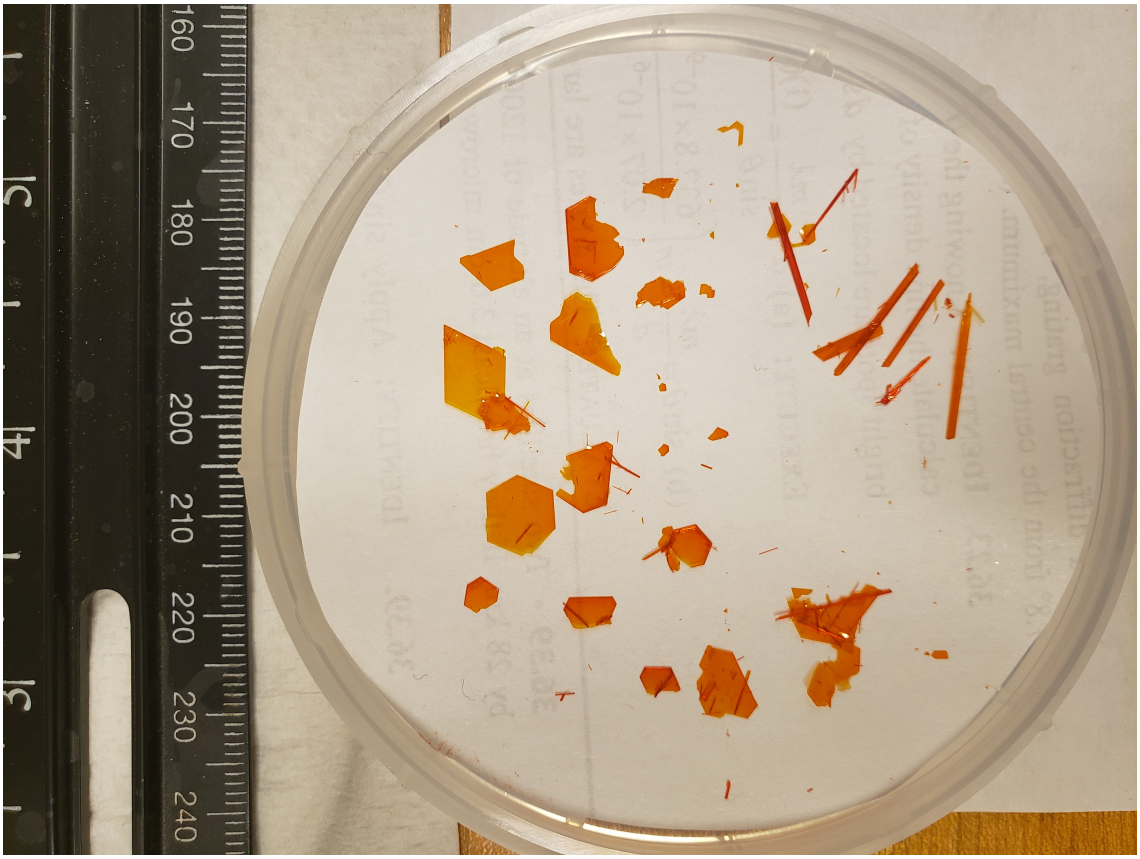

Figure 5: A photo of the typical rubrene "platelets" used in our measurements, visible in the left of the dish. At the upper right, needle-like crystals are also visible. The ruler scale is in mm.

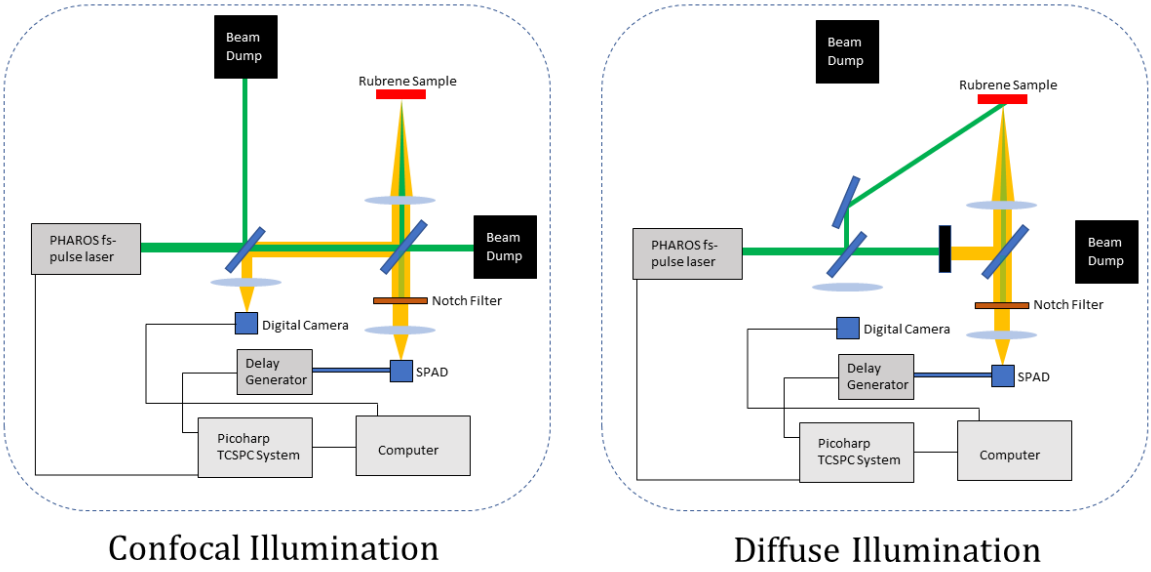

Figure 6: A qualitative diagram of the experimental setup used for photoluminescence measurements. Two experimental configurations are depicted: one in which the crystal is illuminated confocally, and another in which an unfocused laser beam is directed onto the crystal outside of the detection beam path.

months; as noted elsewhere, the oxidation of rubrene crystals at room temperature appears to be light-activated.[21]

3.2 Photoluminescence Measurements

In order to obtain time-resolved photoluminescence data from impulsively excited rubrene single crystals, we used an experimental setup sketched qualitatively in Figure 6. We impulsively excited rubrene crytals using 150-fs pulses from a Light Conversion PHAROS laser, tuning the repetition rate between 5 and 200 kHz. We perform either confocal or diffuse — i.e. unfocused, see Figure 6 — illumination of the crystal. Then, the resulting photoluminescence is collected by a lens and focused directly onto the sensitive area of our detector, a Micro Photon Devices Photon Detector Module-model single photon avalanche diode (SPAD), in order to minimize coupling losses. The dynamics are obtained via a time-correlated single photon counting (TCSPC) technique, discussed in more detail below. As the photoluminescence is free-space coupled into an exposed input window of our detector, we perform

measurements in a darkened room and cover the sample and detector with a cardboard box during measurements. In order to circumvent the "after-pulsing" effect which is exhibited by single-photon-avalanche-diodes [23] and which would otherwise mask our late-time, low-intensity data, we use a Stanford Research Systems DG535 delay generator to gate the signal pulses out of the SPAD. In other words, after the SPAD emits a signal pulse, further pulses are rejected for a time equal to the illumination period, preventing "afterpulses" from appearing in the TCSPC histogram.

Typical time-averaged illumination intensities for diffuse illumination range from $\sim 0.1 - 1$ W/m^2, corresponding to pulse fluences at 5 kHz of 2×10^{-5} to 2×10^{-4} J/m^2. As we generally use b-axially polarized light for illumination, we may use an absorption length of 2.6 μm at 513 nm to calculate peak excitation densities in the range of $2 \times 10^{19} - 2 \times 10^{20}$ m^{-3}. We note that the 200 μs illumination period in these measurements is approximately twice the isolated triplet decay time, so that the calculation of the excitation density from the energy of a single pulse is justified. Earlier work in our group, along with some of the measurements presented in this work, used the confocal illumination technique depicted in Figure 6 and were conducted at repetition rates of 200 kHz. The focused illumination used in this technique had a much narrower beam waist, ~ 40 μm, and consequently pulse fluences were much higher, reaching up to 5×10^{-2} J/m^2.[7] These fluences corresponded to per-shot excitation densities of up to 5×10^{22} m^{-3}; as the repetition period in this case was much shorter than the triplet lifetime, accumulation of excitations from previous shots could have increased the total excitation density by an order of magnitude. At such high excitation densities, the PL signal from geminate triplet fusion is quickly swamped by the nongeminate contribution, preventing the observation of the geminate PL at long ($\sim 1\mu$s) timescales.

3.2.1 Time-Correlated Single Photon Counting

The time-correlated single photon counting (TCSPC) technique is described in great detail in Ref. [24]; we provide a brief summary here. It is first crucial to note that TCSPC is in our case a pulsed-illumination technique, given that it seeks to resolve the dynamics of photoluminescence. The sequence of events during a single measurement cycle is as follows:

1. An illumination pulse is emitted by the light source; this pulse should be short compared to the photoluminescence timescales of interest. For example, our pulses are ≈ 150 fs long, whereas the timescales of interest range from ns to μs.

2. Via either a signal output of the light source or some other method, a timing pulse indicating the start of the illumination arrives at the TCSPC device. This logic pulse does not need to be exactly synchronous with the illumination of the sample, but a high precision in the relative time between the timing pulse and the illumination is crucial.

3. After the arrival of the timing pulse, a timer is started in the TCSPC device.

4. After some time elapses, a photon from the illuminated sample may be detected by the photodetector. This photodetector sends a signal pulse to the TCSPC device. Again, delays between the photon's arrival at the detector and the arrival of the signal pulse are unimportant, but high precision is crucial.

5. Upon the arrival of the signal pulse, the TCSPC device stops the "timer" started by the timing pulse. The resulting time is stored as a photon arrival time.

6. By integrating the above steps over many signal pulses, a histogram containing photon arrival times is "built up" into a probability distribution for photon arrival times, scaled by the total number N of recorded photons.

We note that, in the above account of TCSPC, we specify that the photodetector "may" detect a photon from the illuminated sample. This distinction is crucial. Although a TCSPC technique can achieve very high precision in recording the arrival times of photons (limited by timing error in electronics and the photodetector), the rate at which photon arrivals can be recorded is limited by the time required for the TCSPC system to record a measured photon arrival time. In our system, this time is at least ≈ 90 ns; however, we artificially extend it to be equal to the repetition period using a delay generator, as discussed above. During this "dead time", any subsequent photon signal pulses will be ignored by the TCSPC device.

This limitation can easily lead to a photon arrival histogram which is distorted with respect to the true photoluminescence dynamics. As an extreme example, consider Figure 7. Suppose that the "true" PL dynamics (i.e. probability density of photon arrival times) of a system consist of two sharp "peaks", one at a time arbitrarily denoted as $t = 0$ ns and the other at a time $t = 10$ ns. Suppose that the specifics of photon detection are such that, in any illumination event, there is for each peak a probability $P_1 = P_2 = 0.5$ of a single photon being detected at the photon detector and the resulting signal pulse reaching the TCSPC unit. Suppose further that these two probabilities are uncorrelated, as would (approximately)

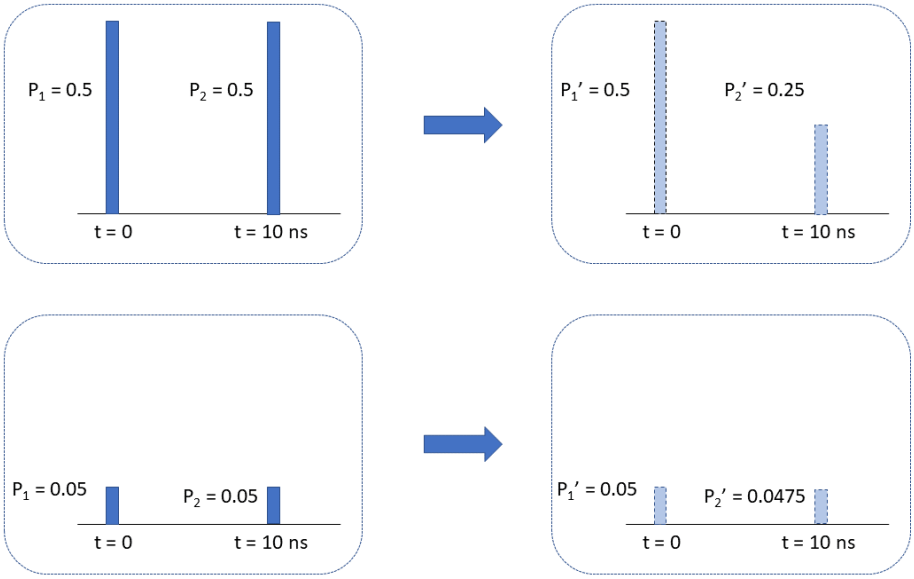

Figure 7: A schematic representation of the true photon dynamics, left, and corresponding detected photon dynamics, right, for a two-peaked photon distribution at different signal levels.

be the case for a system with extremely low detection quantum efficiency.

We now consider the histogrammed dynamics which the TCSPC unit would record. For a given illumination event, there is a probability $P_1 = 0.5$ that the detector will register a photon count during the first peak, and all of these counts will be recorded by the TCSPC unit. There is likewise a $P_2 = 0.5$ probability that the detector will register a photon count during the second peak. However, this count in turn has only a probability $(1 - P_1) = 0.5$ of being recorded; if a count was registered during the first peak, then the dead time will cause this second count to be missed. In a given excitation event, one will then on average record 0.5 counts at $t = 0$ ns and 0.25 counts at $t = 10$ ns. Accordingly, the final histogram after many illumination events will show that peak 1 is twice as high as peak 2, even though both peaks are of equal height in the true PL dynamics.

Consider now a similar example in the case where $P_1 = P_2 = 0.05$. Crucially, this change in the photon detection probabilities for the two peaks need not represent any change in the sample; it could be realized by putting a neutral density filter in the photon detection beam path, for example. In this case, there is in each illumination event a probability $P_1 = 0.05$ that a photon will be detected and recorded at $t = 0$ and a probability $P_2(1 - P_1) =$

$(0.05)(0.95) = 0.0475$ that a photon will be detected and recorded at $t = 10$ ns. In this low-probability regime, we see that the ratio between the heights of peak 1 and peak 2 will be $\frac{1}{0.95} \approx 1.05$, a considerably smaller distortion than in the previous example.

Generalizing to an arbitrary "true" per-illumination photon detection probability density $P(t)$, it is fairly straightforward to see that, given an effective dead time t_D in the TCSPC system after a photon detection and an illumination period T, the effective per-illumination photon detection probability $P^*(t)$ will be bounded by

$$P(t) \geq P^*(t) \geq P(t)e^{-\int_0^t P(\tau)g(t-\tau)\mathrm{d}\tau} \tag{1}$$

where

$$g(\tau) = \begin{cases} 1 & 0 \leq \tau \leq t_D \\ 0 & \tau > t_D \end{cases}$$

We present a simple derivation of the above inequalities in the Appendix. From this form for $P^*(t)$, it is clear that imposing the condition $\int_0^T P(\tau) \ll 1$ will yield $P^*(t) \approx P(t)$. In words, if the expected number of photons detected per illumination event is small, then the probability P_D that, given the detection of a first photon, a second photon is detected during the first's "dead time" is small. This is the motivation for imposing a photon detection rate which is 5% of the laser repetition rate or less.

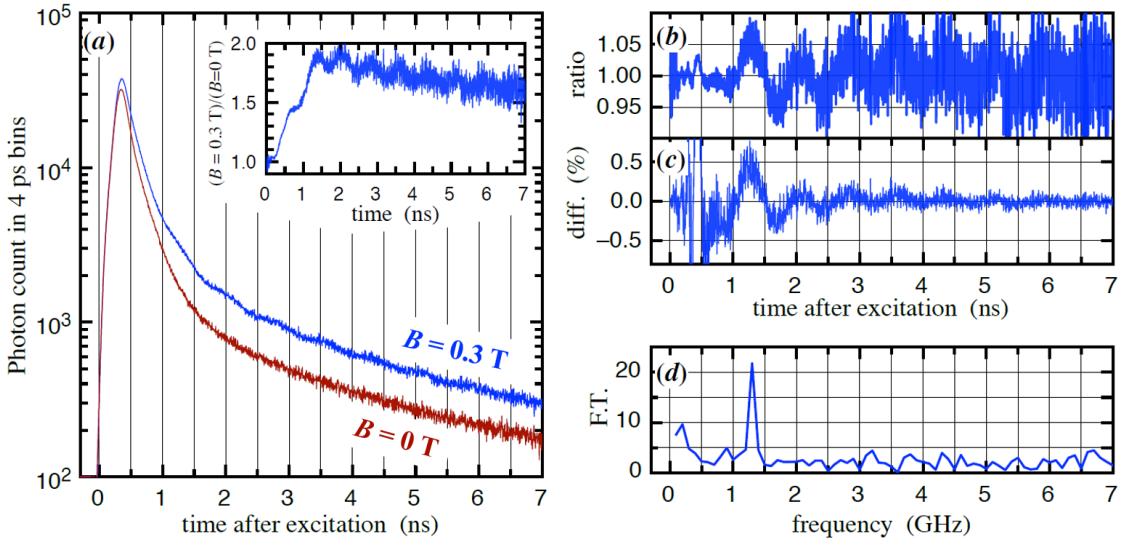

Figure 8: An illustration of a typical quantum beat signature in the photoluminescence dynamics of impulsively excited rubrene. a) depicts the photoluminescence dynamics of a rubrene sample with and without applied magnetic field, with an inset showing the ratio of the two data sets. b) shows the ratio of the magnetic field data from a) to a non-oscillatory model function, essentially "extracting" a sinusoidally oscillating multiplicative factor from the PL dynamics. c) shows the difference between the magnetic field data and this model function, normalized to the peak height. d) shows a Fourier transform of the data in b). Taken from [7].

4 Quantum Beats

4.1 Results

Figure 8 presents a typical quantum beat signature in crystalline rubrene, obtained by applying a $0.3\ T$ magnetic field along the crystalline c-axis. As the figure makes clear, these quantum beats take the form of GHz frequency oscillations superimposed on the photoluminescence dynamics of the sample. Examining subfigures b) and c), we notice that, while the absolute amplitude of the quantum beats (as a percentage of the peak photoluminescence intensity) decays very rapidly, the relative amplitude of the beats (i.e. their magnitude compared to the intensity of a non-oscillating fit to the dynamics, either with a model function or a spline fit) does not visibly decrease before the beats disappear into the noise. Figure 9 illustrates that the frequency of the oscillations which are observed in the rubrene photoluminescence dynamics under high applied magnetic field is dependent on the field orientation.

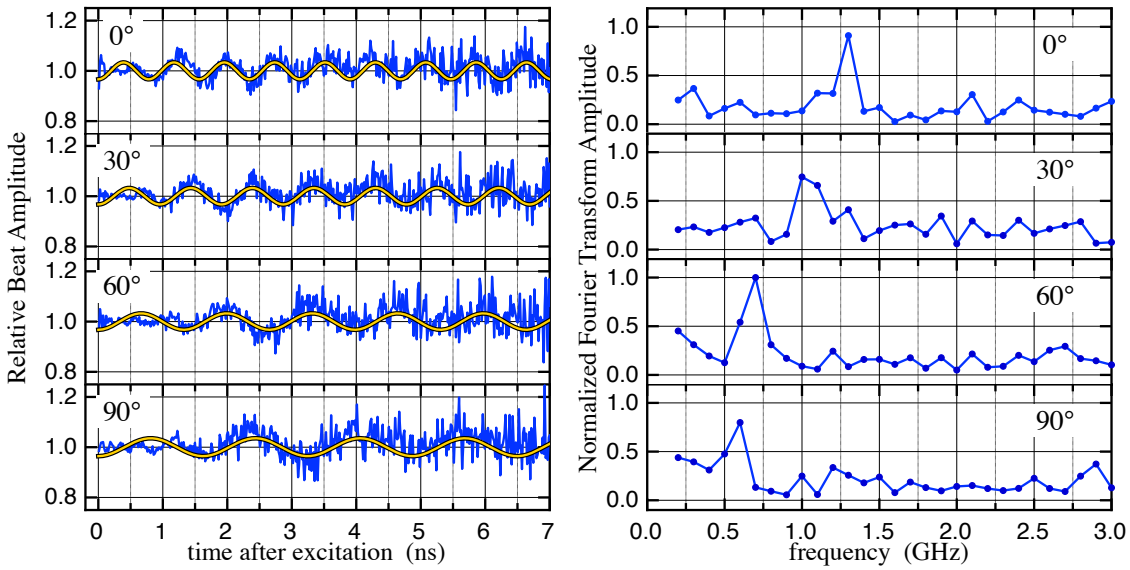

Figure 9: Quantum beat signatures, analogous to plot b) in Figure 8 (left), and Fourier transforms (right) for several different applied field orientations within the *bc* plane. Taken from [7].

For an applied field in the crystalline *bc* plane, frequencies range from 1.3 GHz for an applied field oriented along the *c*-axis to 0.6 GHz for a field oriented along the *b*-axis. This variation is characteristic of quantum beats in organic semiconductors, as noted in the discussion, and supports our determination that the observed oscillations are indeed quantum beats.

In Figure 10, we see a quantum beat signal, as in Figure 8 b), for a *b*-axially oriented magnetic field and measured with long integration times to decrease shot noise. The figure demonstrates the utility of the quantum beat signal as a probe for the spin relationship between triplets; as the beats have a persistence time of at least 30 ns, we may conclude that spin coherence is maintained between the triplet states (which, we note, exist in a room temperature system) for at least this long.

Finally, we note, as illustrated in Figure 11, that altered rubrene samples (i.e. those manifesting a strong 650 nm band in their PL spectra) do not exhibit pronounced quantum beats in their spectrally integrated photoluminescence dynamics. However, when the dynamics of the < 600 nm spectral window are measured, quantum beats like those seen in pristine crystals become apparent.

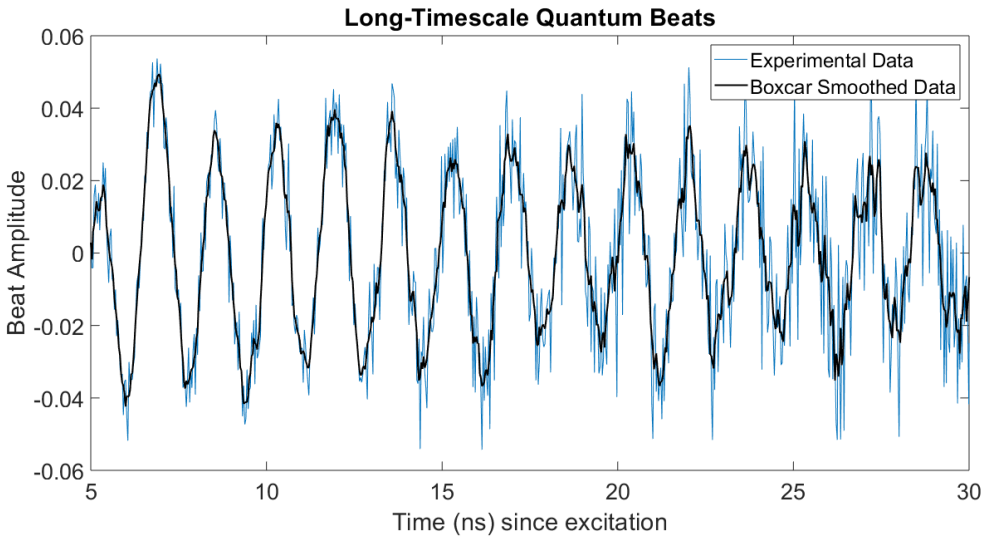

Figure 10: A quantum beat signature for b-axially oriented field.

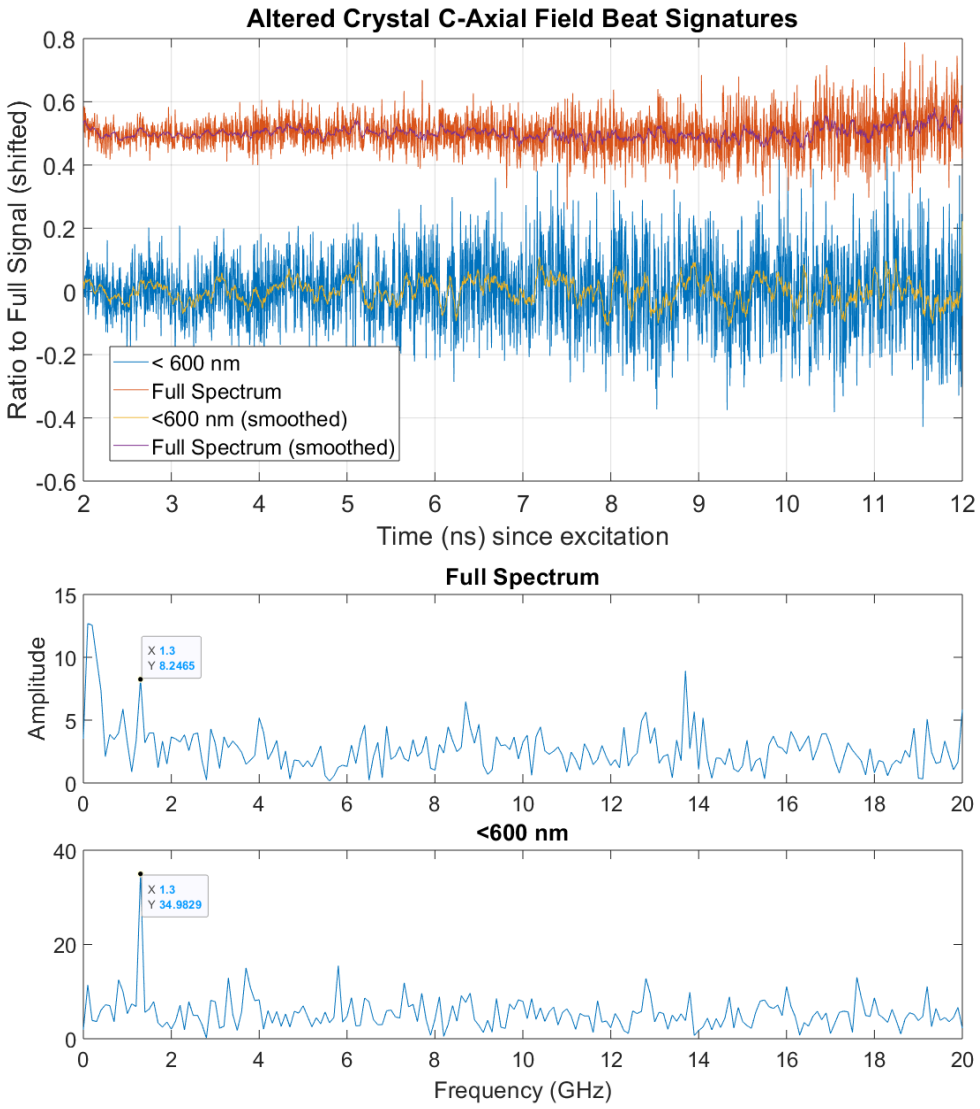

Figure 11: a) Spectrally-resolved quantum beat signatures for an altered crystal with a c-axial applied magnetic field. b) Fourier transform of the beat signatures presented in a).

4.2 Discussion

First observed in tetracene by Chabr et. al. [25], quantum beats (in the context of singlet fission systems) are Ghz-timescale oscillations in the photoluminescence intensity of an impulsively excited sample. Qualitatively, quantum beats are fairly easy to explain; we do so following development outlined elsewhere.[25, 26] Recall the form for the overall singlet state of the triplet pair:

$$|00\rangle = \frac{1}{\sqrt{3}} \left(|1\rangle |-1\rangle - |0\rangle |0\rangle + |-1\rangle |1\rangle \right)$$

Under high magnetic field (i.e. for a Zeeman shift in triplet energies which is much larger than triplet-triplet interactions), this state is not an eigenstate of the Hamiltonian. Ignoring interactions between triplets, the eigenstates with nonzero overlap with the above are

$$|\Psi_1\rangle = |0\rangle |0\rangle , \ |\Psi_2\rangle = |1\rangle |-1\rangle , \ |\Psi_3\rangle = |-1\rangle |1\rangle$$

In high field, Ψ_2 and Ψ_3 will be degenerate with some field strength-independent energy E_2, while Ψ_1 will have a likewise field strength-independent energy E_1. Qualitatively, the field strength-independence of the energy E may be understood as follows: any Zeeman shift in the energy of the triplet state oriented parallel to the field will be "balanced" by the opposite Zeeman shift of the triplet oriented antiparallel to the field. The difference between the energies E_1 and E_2 arises because of a zero-field contribution to the energies of the triplet states $|0\rangle, |1\rangle, |-1\rangle$ from electron-electron interactions within a triplet; crucially, this difference will depend on the orientation of the applied magnetic field with respect to the molecular axes.

If we further assume that some interaction exists between the triplets in the triplet pair, then $|\Psi_2\rangle$ and $|\Psi_3\rangle$ are no longer eigenstates of the Hamiltonian, being replaced by the symmetric combination

$$|\Psi_2'\rangle = \frac{1}{\sqrt{2}} \left(|1\rangle |-1\rangle + |-1\rangle |1\rangle \right)$$

At any rate, elementary quantum mechanics allows us to write the time-evolution of the triplet pair state produced by singlet fission as

$$|\Psi(t)\rangle = e^{i\frac{E_1}{\hbar}t}\left(|0\rangle|0\rangle + e^{i\frac{E_2-E_1}{\hbar}t}(|1\rangle|-1\rangle + |-1\rangle|1\rangle)\right) \tag{2}$$

Given this form, it is straightforward to derive

$$|\langle 00|\Psi(t)\rangle|^2 = \frac{1}{9}\left|e^{i\frac{E_1}{\hbar}}\right|^2\left|\left(1+2e^{i\frac{E_2-E_1}{\hbar}}\rangle\right)\right|^2 = \frac{1}{9}\left[(1+2\cos(\omega t))^2 + (2\sin(\omega t))^2\right]$$

$$|\langle 00|\Psi(t)\rangle|^2 = \frac{1}{9}(5+4\cos(\omega t)) \tag{3}$$

with $\omega \equiv \frac{E_2-E_1}{\hbar}$.

From this simple treatment, we see that the overlap integral between the triplet pair state and an overall singlet state is expected, in high field, to oscillate with a frequency dictated by the energy splitting $E_1 - E_2$. If we assume that the probability for a triplet pair to undergo fusion is proportional to this overlap integral, that the lifetime τ_S of a singlet state (taking into account both radiative relaxation and singlet fission) is short compared to the period $\frac{2\pi}{\omega}$ of the oscillation, and that all of the photoluminescence emitted from the singlet fission material several singlet lifetimes τ_S after impulsive excitation is attributable solely to singlet excitons "re-formed" by triplet fusion, we expect the intensity of this photoluminescence to oscillate with the frequency ω as well.

We note that the above treatment predicts a "contrast" for the quantum beats - that is, a ratio of the sinusoidal amplitude to the non-oscillatory portion of the dynamics - of roughly 40%, far in excess of the contrast of $\sim 5\%$ which we observe e.g. in Figure 8 b). We cannot conclusively explain this discrepancy; it is possible, however, that only a small portion of singlets undergo a coherent fission process (giving rise to quantum beats), while the remainder split incoherently, as suggested in Ref. [27].

5 Geminate Random Walks

5.1 Introduction

As remarked upon earlier, the rapidity with which singlet fission occurs in crystalline rubrene implies that essentially all of the photoluminescence which is emitted more than ≈ 1 ns after excitation is produced by secondary singlet excitons which have been re-formed by triplet fusion. As we analyze this photoluminescence, it is crucial to distinguish between light produced by fusion between geminate and non-geminate triplets.

In particular, we note that nongeminate triplets should, assuming that the percentage of molecules that is excited after impulsive excitation is small, be initially spatially uncorrelated with each other. Neglecting triplet-triplet annihilation effects, they will remain so; at any rate, we expect that the probability per unit time for a given triplet exciton to encounter and fuse with a nongeminate triplet will be proportional to the overall triplet density T: $P_{\text{fuse}} = \gamma T$. It follows that the overall photoluminescence intensity resulting from nongeminate triplet fusion will be proportional to the square of the triplet density: $\text{PL}_{\text{nongeminate}} = \gamma T^2$.

Conversely, a triplet exciton is of course not spatially uncorrelated with its geminate partner; assuming that singlet fission creates triplet states which are on adjacent molecular sites, a geminate triplet pair is initially adjacent, with the spatial relationship between triplet excitons evolving in time in a manner dictated by the nature of their movement through the crystal. We then expect that the probability for a triplet to reencounter and fuse with its geminate partner is some density-independent but explicitly time-dependent function $\alpha(t)$. It follows that $\text{PL}_{\text{geminate}} = \alpha(t)T$.

Given the different scalings of the geminate and nongeminate PL, we see that, for a given triplet density T, there will be some time t, dictated by the dynamics of α, at which the contribution of nongeminate triplet fusion to the overall PL is greater than the contribution of geminate fusion. By decreasing the initial triplet density T_0 produced by the excitation pulse, we may "push back" this timescale in order to probe the geminate dynamics for a longer period of time. This is necessary because only the geminate dynamics contain the explicitly time-dependent factor $\alpha(t)$ which gives information about the spatial evolution of the initially adjacent triplet pair; while the details of triplet diffusion are presumably also encoded in the proportionality constant γ, α is easier to interpret.

In this section, we show long-timescale (up to 200 μ s) dynamics of the photoluminescence of

rubrene single crystals. We find that the early- to intermediate-time portions of the dynamics, which we attribute exclusively to geminate triplet fusion, exhibit power-law behavior which is explainable using a multidimensional random walk model. By studying a transition in this power-law behavior, we are able to estimate the average hopping time for the slowest diffusion dimension as ~ 2 μs.

5.2 Results

In Figure 12, we present the photoluminescence dynamics of an impulsively excited rubrene single crystal at a 5 kHz repetition rate and with an illumination intensity of approximately 0.1W/m^2. We note several features in the data, including a *hump* at $\sim$ 10 ns, a *kink* between two straight-line sections of the data at $\sim$ 100 ns, a *flattening out* at $\sim 10^4$ ns, and a *downward bend* at $\sim 10^5$ ns.

We first consider the *hump*. The prominence of this feature is sample-dependent, and it is much more prominent in the $>$ 650 nm portion of the photoluminescence than it is in the $<$ 600 nm portion, as shown in Figure 13. Accordingly, we assign it to the "altered" photoluminescence remarked upon above, and we disregard it going forward. The *flattening out* at $\sim 10^4$ ns is, as shown in Figure 14, intensity dependent, occurring earlier at higher illumination intensities. In light of the discussion above, we attribute this *flattening* to the nongeminate PL becoming the dominant contribution to the PL. As shown in the same figure, the late time *downward bend* can be well-fitted by an exponential decay with a time constant of $\tau \approx 60$ μs. As the nongeminate PL signal is proportional to the square of the triplet density, this is consistent with an exponential decay of the triplet population with a time constant of 100 ± 20 μs, as reported in Ref. [6].

We now turn our attention to the *kink* at $\sim$ 100 ns. We note that this kink occurs between two straight-line sections on the log-log plot, corresponding to a power-law decay in the photoluminescence intensity. As shown in Figure 15, the dynamics before and after this *kink* can be well-fitted by power laws with exponents of -1.18 ± 0.02 and -1.66 ± 0.03, respectively. We note that the quoted errors are from shot noise; while the background subtraction introduces an additional error, it is comparatively small. These two exponents differ, within the experimental error, by -0.5, and both are relatively close to values of -1 and -1.5, respectively. This "transitioning" power law behavior, along with the exponents and the difference between them, is consistent across multiple rubrene samples. It can, as

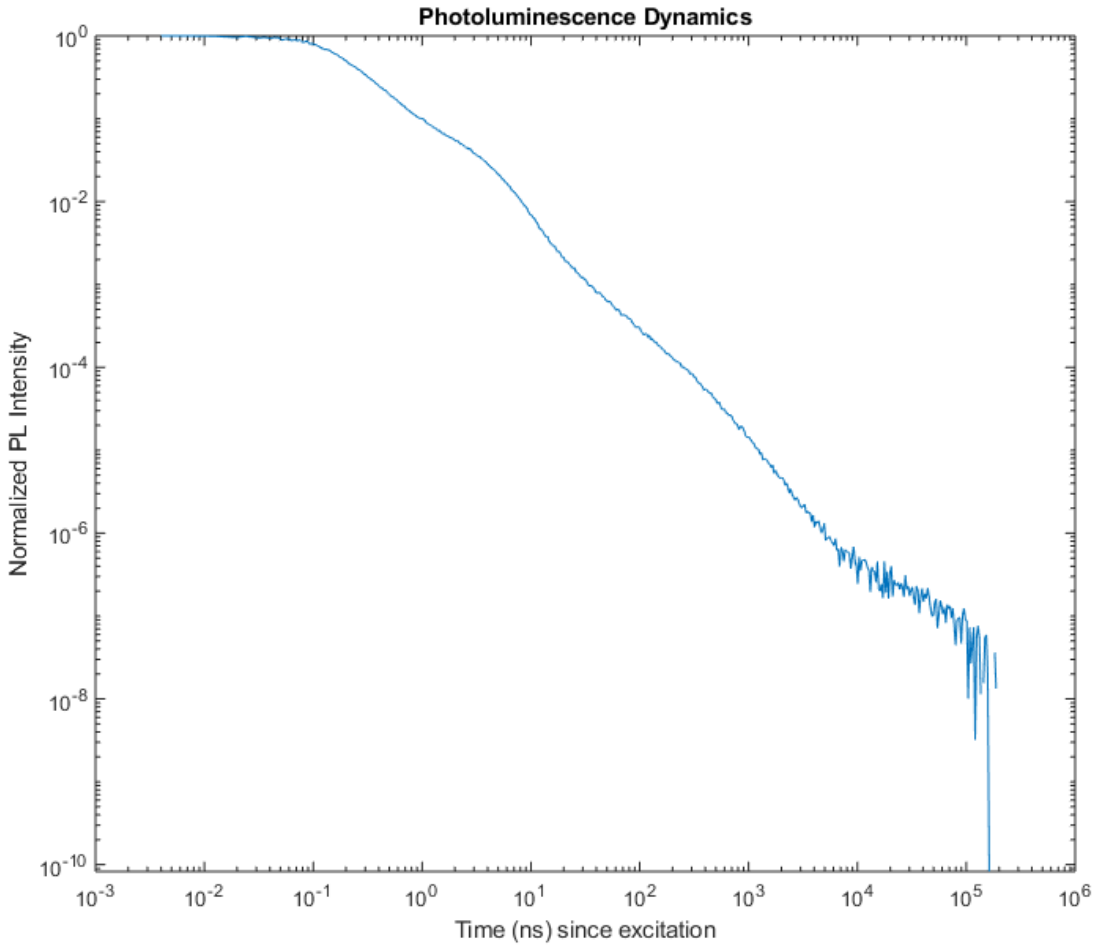

Figure 12: Log-log plot of photoluminescence dynamics of an impulsively excited rubrene single crystal at an excitation density of 0.12 W/m^2. A background subtraction has been performed. Note the various features in the data: a *hump* at ~ 10 ns, a *kink* at ~ 100 ns, a *flattening out* at $\sim 10^4$ ns, and a *downward bend* at $\sim 10^5$ ns.

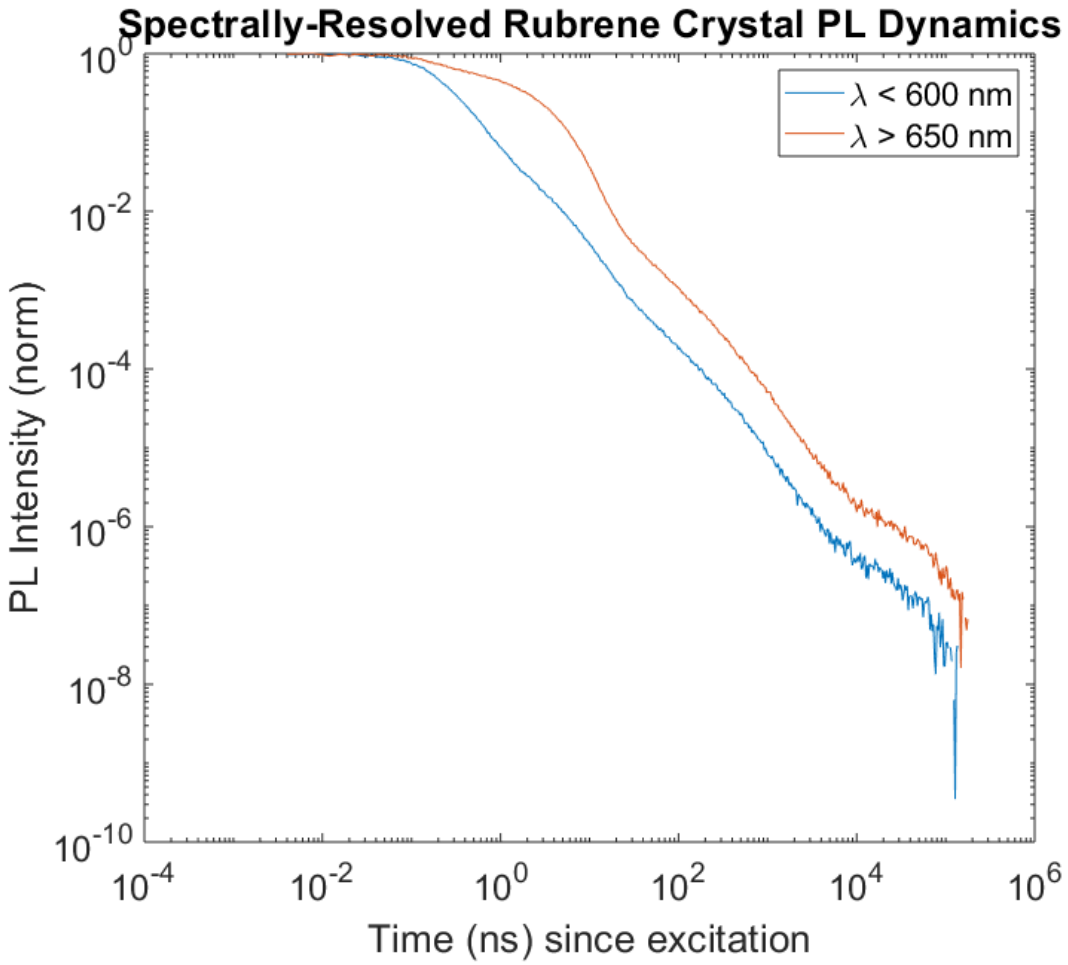

Figure 13: Spectrally-resolved dynamics for an impulsively excited rubrene crystal. Note the smaller prominence of the *hump* at ~ 10 ns in the < 600 nm window.

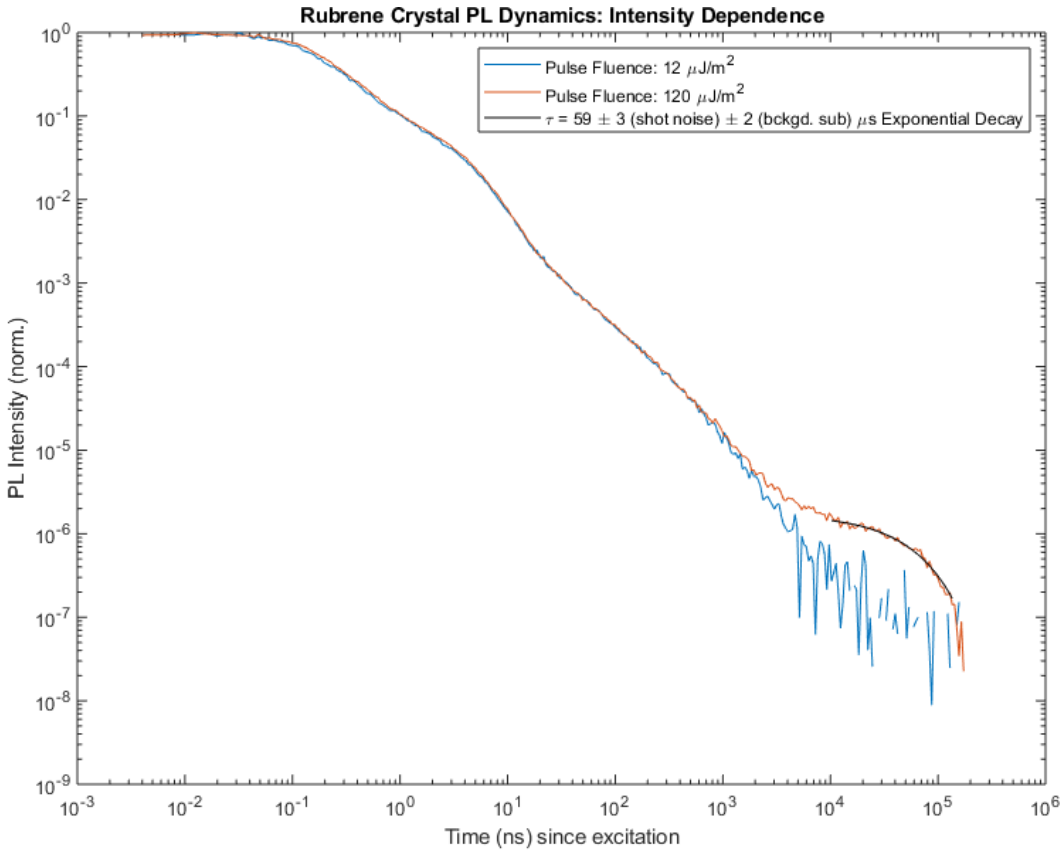

Figure 14: Normalized photoluminescence dynamics of an impulsively excited rubrene crystal for different illumination intensities. Note the earlier onset and higher signal level (relative to the intensity peak) of the late-time *flattening out* at higher intensity.

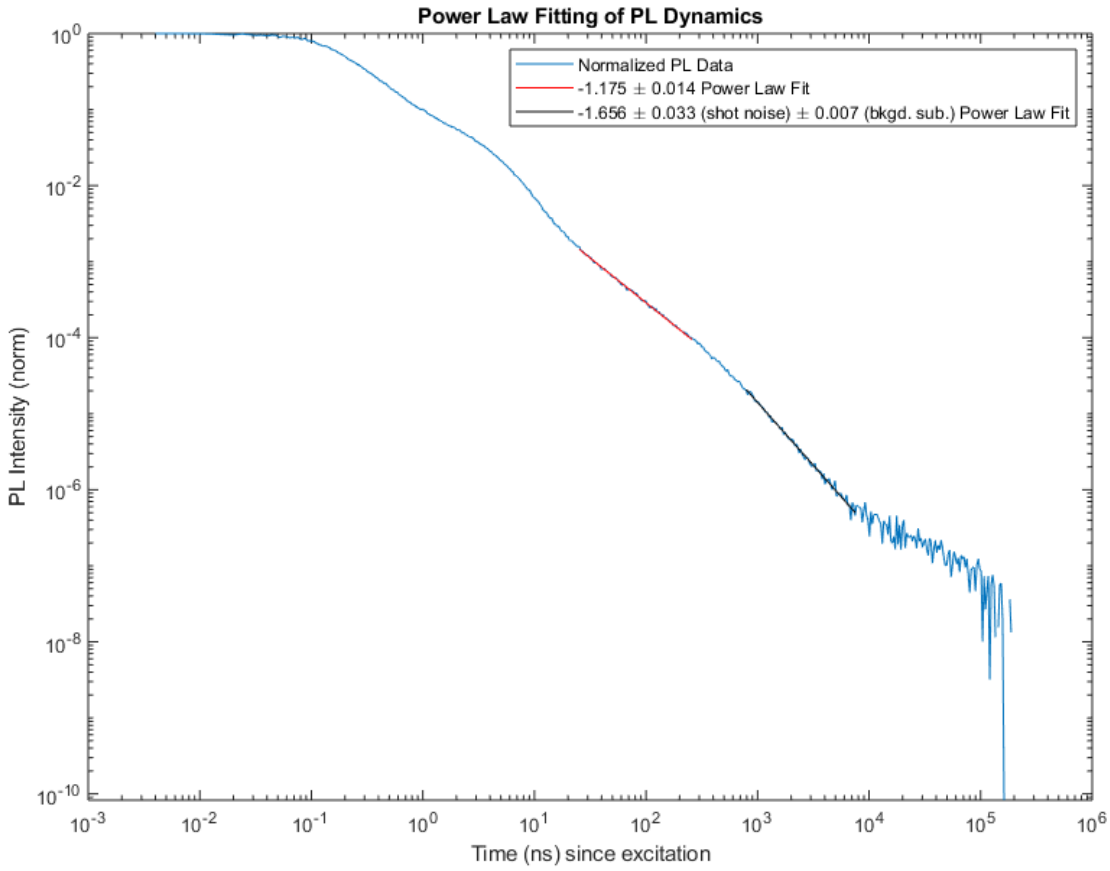

Figure 15: Power law fits to the normalized photoluminescence dynamics displayed in Figure 12.

we show, be well-explained in the context of a random walk model.

5.3 Mathematical Background

5.3.1 Development of Random Walk Model

Consider a d-dimensional rectangular lattice; suppose that a random walker is initially at the origin at time $t = 0$. Suppose further that the random walker takes independent hops along the i-th axis at an average rate R_i, so that the total number of hops is Poisson distributed. Assume that each of these hops changes the ith coordinate by ± 1, with both possibilities equally probable. We consider the probability $P(t)$ that the random walker is at the origin at time t; note that we do not assume that the random walker has returned to the origin for the first time. Let $P_i(t)$ express the probability that the ith coordinate of the random walker is 0 at time t. It follows that, assuming that the "hops" along different dimensions are uncorrelated,

$$P(t) = \prod_{i=1}^{d} P_i(t) \tag{4}$$

It is known that, for a one-dimensional isotropic random walker (i.e. one for which leftward and rightward movement are equally probable), the probability $P^*(n)$ for the random walker to have returned to the origin after precisely n hops, with n even, is asymptotically proportional to $\frac{1}{\sqrt{n}}$; a proof of this claim is given in the appendix. Since the total number of hops at a given time $n_i(t)$ is Poisson distributed, we know that $\langle n_i(t) \rangle = R_i t$. Defining $\tau_i = \frac{1}{R_i}$, we may for $t \gg \tau_i$ take $n_i(t) \approx R_i t$; for large t, $n_i(t)$ will be approximately Gaussian distributed around $R_i t$ with a standard deviation of $\sqrt{R_i t}$ which is small in comparison to the expected value. Let, then, $n_i(t) = R_i t$ for $t \gg \tau_i$. We can then write

$$P_i(t) \approx P^*(n_i) \propto \frac{1}{\sqrt{n_i}} \propto \frac{1}{\sqrt{t}}$$

Conversely, in the case where $t \ll \tau_i$, we may to zeroth order write $P_i(t) \approx 1$; the exact form of $P_i(t)$ for small t will be given later. This leads to an interesting phenomenon in the dynamics of $P(t)$, the overall return probability. Suppose that we choose t (and have suitable hopping constants R_i) such that $\tau_1, \tau_2, \ldots \tau_n \ll t \ll \tau_{n+1}, \tau_{n+2}, \ldots \tau_d$. Then we will have $P_1(t) \approx \frac{A_1}{\sqrt{t}}$, $P_2(t) \approx \frac{A_2}{\sqrt{t}}, \ldots, P_n(t) \approx \frac{A_n}{\sqrt{t}}$, $P_{n+1}(t) \approx 1$, $\ldots P_d(t) \approx 1$. It follows that

$$P(t) = \prod_{i=1}^{d} P_i(t) = \prod_{i=1}^{n} P_i(t) \prod_{i=n+1}^{d} P_i(t) = At^{-\frac{n}{2}} \tag{5}$$

where $A = A_1 A_2 \dots A_n$. Notice that $P(t)$ exhibits power-law scaling with t, but that the exponent of this scaling depends on the number of hopping dimensions for which $\tau_i \ll t$. If, for example, we chose $\tau_1, \tau_2, \dots \tau_d \ll t$, we would have $P(t) \propto t^{-\frac{d}{2}}$. Conversely, if $\tau_1 \ll t \ll \tau_2, \dots \tau_d$, we would have $P(t) \propto t^{-\frac{1}{2}}$.

From this, we conclude that, in a random walk system where the hopping rates R_i differ by orders of magnitude, we will see "transitions" in the power-law scaling of the return probability $P(t)$, with the power law gaining a factor of $\frac{1}{\sqrt{t}}$ each time the time t increases beyond one of the characteristic hopping timescales τ_i and hopping along a certain dimension becomes effective. We devote the next section to the modeling of these transitions in order to determine the time constants τ_i given $P(t)$.

5.3.2 Power Law Transitions in a Symmetric Multidimensional Random Walk

We begin by writing explicitly a power series representation of $P_i(t)$. Let $H_i^k(t)$ denote the probability that, after a time t, the random walker has taken exactly k hops along the ith hopping axis. As the number of hops is Poisson distributed, this probability is given by

$$H_i^k(t) = \left(\frac{t}{\tau_i}\right)^k \frac{1}{k!} e^{-\frac{t}{\tau_i}} \tag{6}$$

Likewise, let G_k denote the probability that an isotropic random walker, initially at the origin, returns to the origin after exactly k hops. As remarked upon in the appendix, we know that

$$G_k = \begin{cases} 0 & k \text{ odd} \\ 2^{-k}\binom{k}{\frac{k}{2}} & k \text{ even} \end{cases} \tag{7}$$

Then $P_i(t)$ admits a simple representation in terms of the two probabilities given above:

$$P_i(t) = \sum_{k=0}^{\infty} G_k H_i^k(t) \tag{8}$$

It is a fairly straightforward exercise to rearrange this into a power series in terms of $\left(\frac{t}{\tau_i}\right)$; we reserve these manipulations for the appendix, and we merely quote the final result here:

$$P_i(t) = \sum_{m=0}^{\infty} C_m \left(\frac{t}{\tau_i}\right)^m \tag{9}$$

where

$$C_m = (-1)^m \sum_{k=0}^{\lfloor \frac{m}{2} \rfloor} \left(\frac{1}{2}\right)^{2k} \frac{1}{(m-2k)!(k!)^2} \tag{10}$$

This power series representation is valid for all values of t; as convergence is slow, however, it is most useful when $t <\sim \tau_i$. We emphasize that the power series coefficients are fixed by random walk theory, so that the only free parameter is τ_i.

With this in mind, we can schematically illustrate how a hopping timescale τ_i may, under certain conditions, be extracted from the return probability $P(t)$ for a symmetric anisotropic random walk. Suppose that we have a d-dimensional random walk such that $\tau_1 \leq \tau_2 \leq \ldots \tau_{d-1} \ll \tau_d$. We will then observe a transition in the power-law behavior of $P(t)$ from an exponent of $-\frac{d-1}{2}$ to $\frac{-d}{2}$; this transition will occur on a timescale dictated by τ_d, which is of course not known a priori. τ_d can, however, be found to order of magnitude by estimating the transition location; in particular, if one restricts one's attention to the portion of the dynamics of $P(t)$ which is well-fitted by the power law $P(t) = At^{-\frac{d-1}{2}}$, one can be assured that one is in a regime where $t \ll \tau_d$. In this regime, again,

$$P(t) = P_d(t) \prod_{i=1}^{d-1} P_i(t) = P_d(t) \left(At^{-\frac{d-1}{2}}\right) \approx At^{-\frac{d-1}{2}}$$

Meanwhile, in a regime where $t <\sim \tau_d$,

$$P(t) = P_d(t) \left(At^{-\frac{d-1}{2}}\right) \tag{11}$$

where, crucially, the constant A is unchanged. By performing a power law fit to the dynamics of $P(t)$ in the $t \ll \tau_d$ regime, one can extract the constant A. Dividing $P(t)$ by this fit in the $t \lesssim \tau_d$ regime, then, gives

$$\frac{P(t)}{At^{-\frac{d-1}{2}}} = P_d(t)$$

In other words, it is possible to extract the return probability P_d of the random walker along the dth dimension by dividing the mid-transition dynamics of $P(t)$ by a power-law which appropriately fits the pre-transition dynamics. Once $P_d(t)$ is known, it is straightforward to find τ_d by fitting $P_d(t)$ with the power series representation from Equations 9 and 10, appropriately truncated.

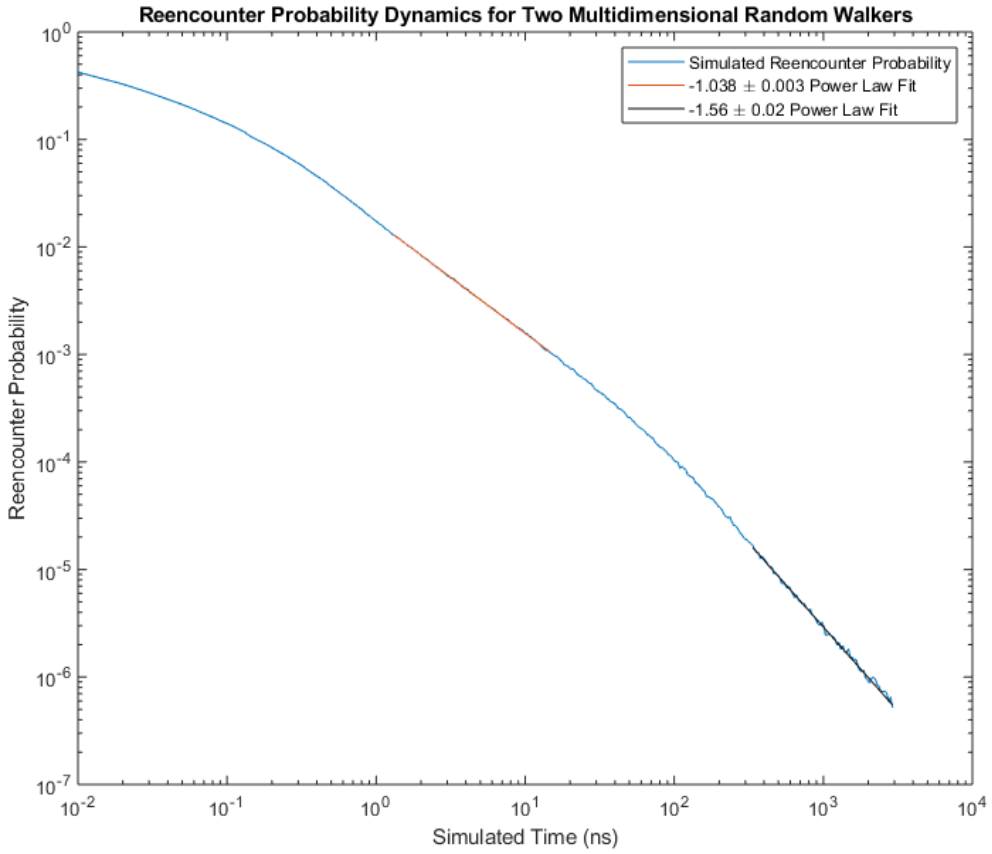

Figure 16: A log-log plot of the simulated reencounter probability for two random walkers. The fastest per-triplet hopping time, $\tau_1 = 0.01$ ns, was the discrete timestep for the simulations. Other timescales were $\tau_2 = 3.7$ ns and $\tau_3 = 370$ ns; τ_3 was chosen as $100\tau_2$ so that the different hopping timescales were well resolved. Note that straight-line sections of the plot correspond to power-law behavior.

5.3.3 Simulation Results

In order to verify the claims above, we perform discrete-time, Monte Carlo random-walk simulations modeling the reencounter probability between two particles in a three-dimensional rectangular lattice. Note that, while the development above focused on the return probability for a single random walker, the two cases can be seen to be essentially equivalent. In particular, if we take the origin to be comoving with one of our random walkers, the relative position of the other can be described by a random walk in which all of the per-walker hopping rates R_i are doubled.

As Figure 16 makes clear, the power-law behavior for the reencounter probability predicted by random walk theory is exhibited by the simulations. Moreover, the simulations exhibit the expected transition from power law dynamics with a log-log slope of approximately -1.0 (characteristic of a 2D walk) to dynamics with a slope of -1.5 as the third hopping dimension becomes effective on a timescale dictated by $\frac{\tau_3}{2}$, the effective hopping rate of one triplet relative to the other along the slowest axis. The exact location of this transition is perhaps unexpected - note that the data has "bent" into the later-time power law by ~ 200 ns. To confirm that the specifics of the transition are as predicted by the theory, we fit the transition as described in the preceding section.

In particular, we divide the reencounter probability in a region around $\sim$ 200 ns by an extrapolation of the -1.0 power law fit (red curve in Figure 16) performed to the earlier dynamics. We then fit the resulting ratio data with the power series representation in Equations 9 and 10, truncated at 9th order. Possibly because of issues with the fitting of the early-time power law, it is necessary to introduce a small constant offset to this power series representation as a free parameter in order to replicate the ratio data. In particular, note that the ratio data in Figure 17 would, if extrapolated to $t = 0$, be greater than 1; since the ratio should in principle be equal to $P_3(t)$ and hence less than 1, this indicates that our fitting procedure overestimates the ratio at early times. Beyond this, however, agreement is good. Moreover, the calculated time constant $\tau = 191 \pm 11$ ns in this fitting is, within the fitting error, equal to the expected value $\frac{\tau_3}{2} = 185$ ns. We remark also that the fit was performed without prior knowledge of the value of τ_3.

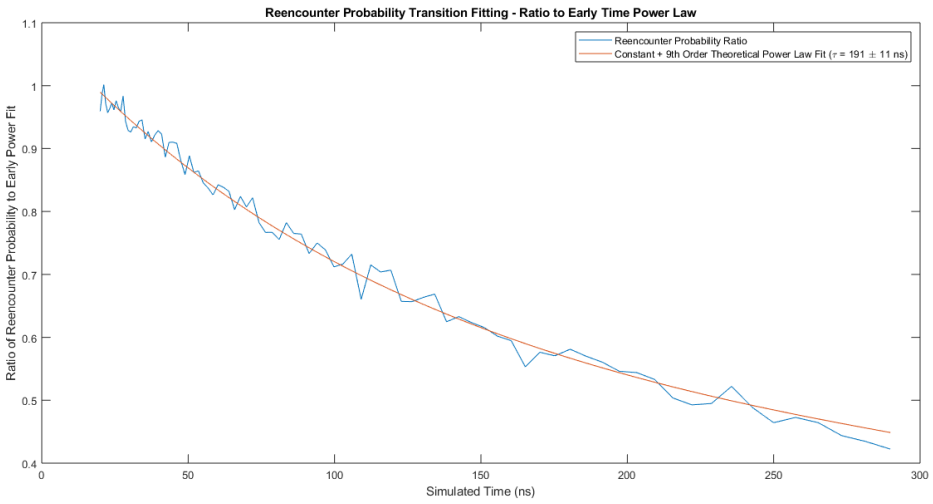

Figure 17: Fitting of the "transition" of the reencounter probability from a -1.0 to a -1.5 power law. The fit was performed using the power series given in Equations 9 and 10, truncated at 9th order and with the addition of a free constant offset.

5.4 Application to Rubrene

We now seek to apply our random walk model to rubrene. In keeping with the fast singlet fission time reported elsewhere [5, 4], we know that all of the photoluminescence emitted by a rubrene crystal more than $\sim$ 1 ns after excitation is produced by triplet fusion and radiative relaxation of the resulting singlet. We assume that triplet fusion can only occur when two triplets are adjacent in the rubrene lattice, i.e. on nearest molecular neighbors. The probability of fusion between geminate triplets, and hence the geminate photoluminescence intensity, should then be proportional to the time-dependent probability $\alpha(t)$ for two initially adjacent triplet excitons to again be adjacent at time t.

Let us assume that the individual triplets undergo independent multidimensional random walks in the lattice with hopping rates R_1, R_2, R_3 along each of the crystal axes. If we use a coordinate system which comoves with one of the diffusing triplets, the problem of finding the reencounter probability $\alpha(t)$ reduces to finding the probability $p(t)$ for a single random walker to return to the origin, with two caveats. The first is simple: the effective hopping rates R_1', R_2', R_3' in this single-walker picture are related to the per-triplet hopping rates by $R_i' = 2R_i$, and hence $\tau_i' = \frac{1}{2}\tau_i$.

The second is more subtle. In the random walk literature, (e.g. [28, 29]) it is common to cite two probabilities: the probability $f(t)$ that a random walker returns to the origin *for the first time* at time t, and the probability $p(t)$ that a random walker has returned to the origin at time t (not necessarily for the first time). The distinction is an important one; for example, in $1D$, the asymptotic behavior of the two probabilities differ, with $f(t) \propto t^{-\frac{3}{2}}$ in comparison to $p(t) \propto t^{-\frac{1}{2}}$, as discussed before.[28, 29] Likewise, a relation analogous to equation 4 will not hold for the first return probability $f(t)$ of a multidimensional walk.

Let us suppose that, whenever two randomly walking rubrene triplets reencounter each other, there is some probability γ that the two triplets re-fuse and emit a photon, ending the random walk. If we transition to a discrete time picture which replaces the time t with the number of hops n, we may define a probability $p_\gamma(n)$ as follows: $p_\gamma(n)$ is the probability that a random walker will be at the origin after a total of n "hopping times" have passed, given that there is a probability γ that the random walker is annihilated whenever it returns to the origin. Intuitively, we can see that $p_0(n) = p(n)$, since here the chance for annihilation to occur is 0. Likewise, we can see that $p_1(n) = f(n)$. In general, we have the recursive formula

$$p_\gamma(n) = f(n) + (1-\gamma)\sum_{j=1}^{n-1} f(j)p_\gamma(n-j) \tag{12}$$

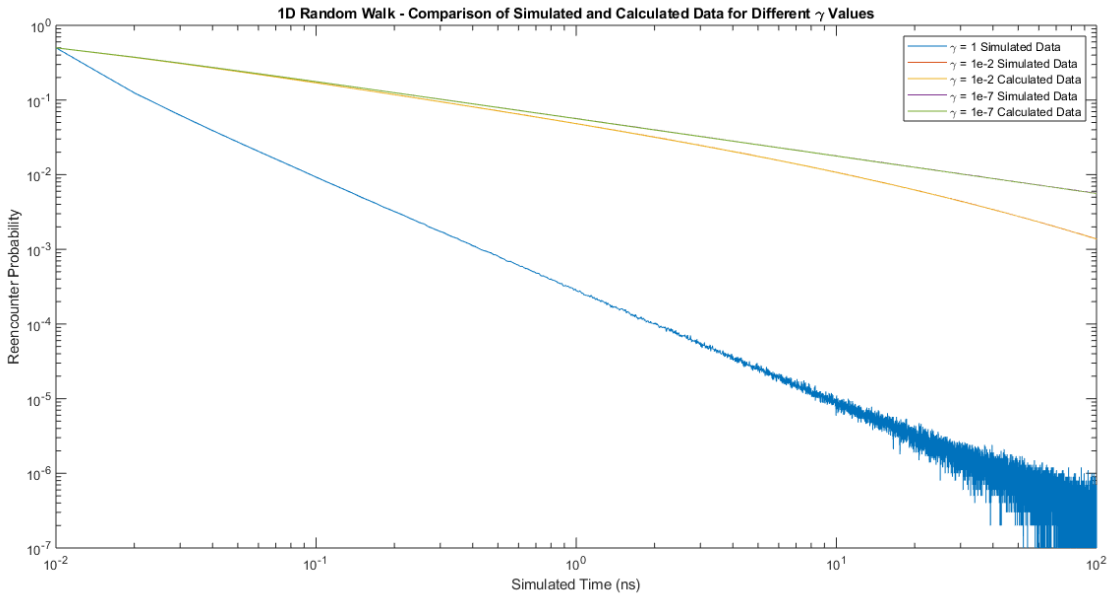

Figure 18: A comparison of the calculated and simulated return probabilities $p_\gamma(n)$ for a 1D random walk and various values of γ. Note that there are a total of 5 curves, but only 3 are visible because of the good agreement between the simulations and the calculation.

which we note differs from a formula given for $p(n)$ in Ref. [29] only by the addition of a factor of $(1-\gamma)$. In order to validate this formula, we present in Figure 18 a plot of simulated vs. calculated return probabilities p_γ for a 1D random walk; note that the simulated and calculated return probability curves overlap, indicating very good agreement.

It is then clear that the reencounter probability $\alpha(t)$ for the triplet pair is not modeled exactly by $p(t)$ for a random walk, but rather by $p_\gamma(t)$. We now justify the choice to model $\alpha(t)$ using $p(t)$. In Ref. [16], measurements of the (time-integrated) photoluminescence yield of rubrene crystals relative to illumination intensity observed two linear regimes, one at low intensity and one at high intensity, separated by at least a factor of 10.

We interpret these two linear regimes as follows. In the low-intensity linear regime, separations between photoexcited singlets are sufficiently large that triplet fusion can essentially occur only between *geminate* triplets. The probability for a triplet to fuse with its geminate partner and emit light at some point before it decays is some density-independent

constant β, dictated by the specifics of triplet diffusion and the decay time; accordingly, the photoluminescence yield is linear in the intensity. In the high-intensity regime, collisions between nongeminate triplets become so frequent that the probability for a triplet to undergo fusion and emit light is essentially unity (limited possibly by any non-radiative routes for triplet-triplet annihilation), and the photoluminescence yield is again linear in the intensity.

The factor of at least $10\times$ difference between these regimes would indicate that β is no greater than 0.1, so that no more than 10% of geminate triplets annihilate each other before the triplets decay individually. As the deviation of $p_\gamma(t)$ from $p(t)$ occurs because of the chance that triplets annihilate, we argue that $p(t)$ should be close to $p_\gamma(t)$ during the timescales of interest. Naively, we would expect to have the bound $0.9p(t) \leq p_\gamma(t) \leq p(t)$. In particular, we would expect that p_γ is bounded below by the product of the "annihilation-free" return probability $p(t)$ with the probability that a triplet has survived until a time t. This latter probability is in turn bounded below by 1 minus the probability that a triplet undergoes geminate annihilation during its lifetime, whence we get the lower bound above. Unfortunately, as Figure 19 shows, this bound does not hold in general: it is possible for p_γ to drop below the product of $p(t)$ and the triplet survival probability. Nonetheless, we assume that our basic insights about $p(t)$, including the dimensional transition analysis above, remain valid for p_γ.

With this in mind, we present in Figure 20 the results of fitting the power law transition of the data in Figure 15 using the power series form presented in Equations 9 and 10, plus a constant offset. This fit yields a time constant $\tau_3' = 1.1 \pm 0.4$ μs for the effective hopping time along the slowest axis; as discussed above, this corresponds to a per-triplet hopping time of $\tau_3 = 2.2 \pm 0.8$ μs. We note that hopping is already two-dimensional long before τ_3 is reached, since the power law dynamics before this time have a slope of -1.0, characteristic of 2D hopping. In principle, we could extract τ_2 in a similar way to τ_3 by fitting a transition from -0.5 to -1.0 power law behavior; however, this transition is not well-resolved in our data.

Using a value of 7.18 Å for the lattice constant along the b-axis [14], and noting that the diffusion length along this axis is 4 μm [17] given a triplet lifetime of 100 μs [6], we estimate a per-triplet hopping rate

$$\tau_1 \sim (100\ \mu\text{s}) \left(\frac{7.18\ \text{Å}}{100\ \mu m} \right)^2 \sim 3\ \text{ps}$$

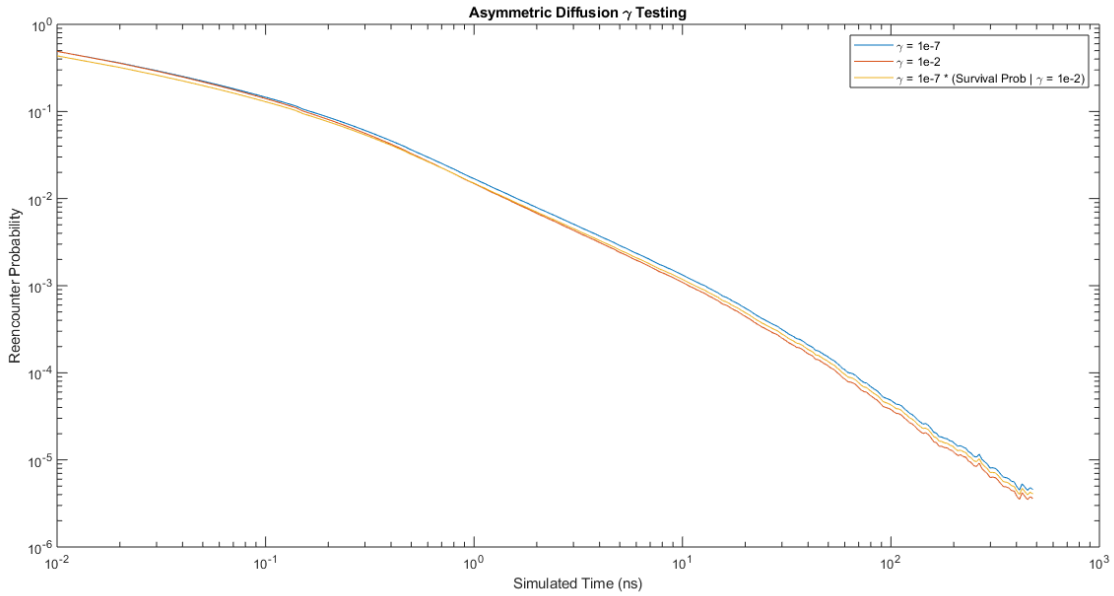

Figure 19: A figure comparing the return probability $p_{0.01}(t)$ (red) to $p_{1e-7}(t)$ (blue, essentially equal to $p(t)$) and to $p_{1e-7}(t)$ times the probability that the pair of random walkers survives until the end of the simulation, given that $\gamma = 0.01$ (yellow). The per triplet hopping times are $\tau_1 = 0.01$ ns, $\tau_2 = 1$ ns, and $\tau_3 = 100$ ns. Note that the red curve falls below the yellow curve by the end of the data.

It is worth noting that the hopping time τ_3 along the lowest-mobility axis is approximately six orders of magnitude larger than this fast hopping time, demonstrating the extreme anisotropy of triplet diffusion in rubrene.

We remark that the method described here does not allow us to determine which crystalline axis this long hopping time τ_3 is associated with. However, we may consider the calculations of electronic coupling between molecules given in Ref. [30] — note that this reference uses a sign convention in which the a and b axes are switched. These calculations show the largest electronic coupling along what we call the crystalline b-axis, along with a smaller but non-negligible coupling along a direction d which lies in the ab plane. All other couplings are said to be negligible. Assuming that the triplet hopping times depend on these couplings, this result implies that the hopping times τ_a, τ_b, and τ_c obey the inequality

$$\tau_b < \tau_a < \tau_c$$

This suggests that the time τ_3 which we have calculated corresponds to hopping along the crystalline c-axis.

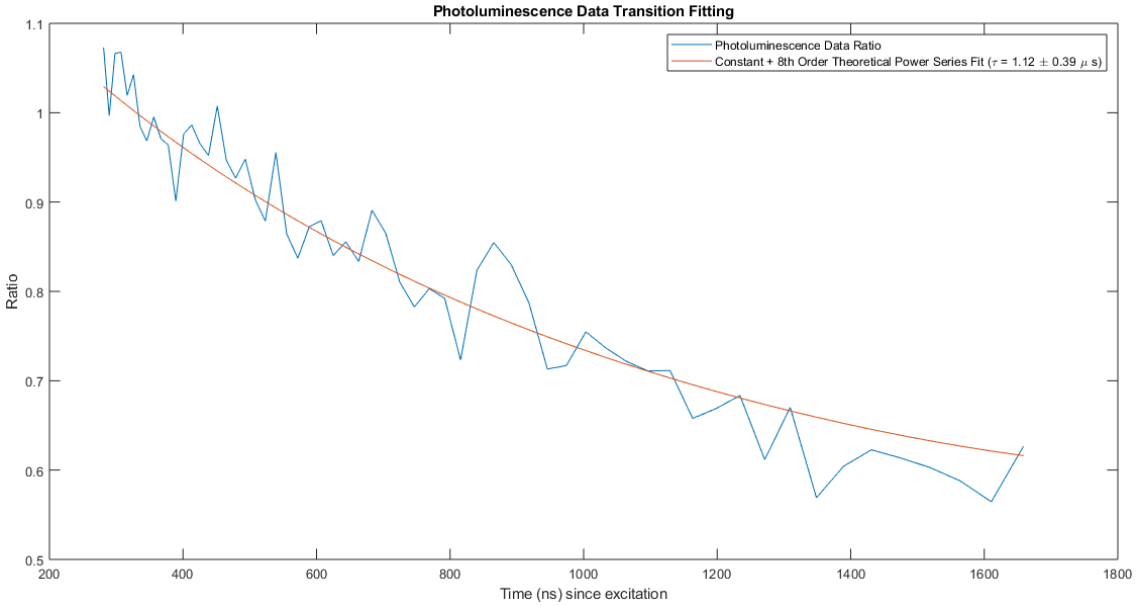

Figure 20: An analogous figure to Figure 17, this time with the experimental photoluminescence intensity data and corresponding early time power law fit as depicted in Figure 15. The ratio data is once again fitted by equation 9, this time truncated at 8th order, plus a constant offset.

6 Synthesis and Conclusions

It is worth noting a few conclusions which may be drawn from the experimental results above. In particular, recall from Figure 10 that the quantum beat signal in rubrene lasts for at least 30 ns, establishing a spin coherence time between geminate triplets that lasts at least this long. As Figure 15 illustrates, the ~ -1 power law slope in the data, characteristic of 2D triplet diffusion, has already begun by the end of this 30 ns period; this suggests that spin coherence is maintained even after triplets separate from each other and begin to diffuse independently within crystal planes, which is noteworthy given that such diffusion involves many "hops" between molecules.

Additionally, the observation that the quantum beat signal stays relatively constant as a fraction of the overall PL signal during this time suggests that the large discrepancy between the theoretically predicted and observed magnitudes of the quantum beat signal cannot be explained by invoking two populations of triplet pairs with different dynamics, e.g. one population whose triplet pairs remain in close proximity, maintain coherence, and produce quantum beats while another population has triplets separate and lose their phase relationship. In particular, in such a model, we would expect the quantum beat signal to substantially grow or shrink as one or the other population became the dominant contributor to photoluminescence, contradicting the observations in Figure 10.

In conclusion, time-resolved photoluminescence studies of impulsively excited rubrene crystals, coupled with appropriate analysis, can reveal significant information about the intermediate- to long-timescale dynamics of triplet excitons within the material, provided an appropriate distinction is made between the contributions of geminate and nongeminate triplet fusion to the photoluminescence signal. In particular, the quantum beat measurements described in this work give insight into the spin relationship between triplets, including their at least 30 ns spin coherence time. Likewise, the power-law transition measurements give insight into the spatial relationship between triplets, demonstrating the extreme anisotropy of triplet diffusion in the rubrene crystal and allowing the slowest hopping time, which would be completely inaccessible to the technique used to determine the fastest hopping time, to be estimated at $\tau_3 = 2$ μs. The analysis of these latter measurements also demonstrates a general approach for determining hopping times in highly anisotropic random-walk processes by fitting the transitions between power-law dynamics of different slopes which these processes will exhibit.

7 Acknowledgements

The author wishes to thank Prof. Ivan Biaggio for his support as a research advisor and for his willingness to allow a first-year undergraduate into a lab full of fragile equipment. Likewise, he wishes to thank Drew Finton for his diligence in showing him the ropes in lab - and in reading through excessively lengthy learning homeworks as a PHY 021 TA. He wishes to thank Lauren Dallachiesa for valuable conversations, physics-related and otherwise, and acknowledges the considerable patience of the entire group during lengthy and specialized back-and-forths in group meeting. He is grateful to the Lehigh University physics department for the incredible access and support he has received during his time as an undergraduate at Lehigh, and he acknowledges the tremendous academic freedom he was given as a member of Lehigh's Eckardt Scholars program.

8 Appendix

8.1 Derivation of Formula for TCSPC Photon Dynamics Distortion

We present here a derivation of Equation 1, reproduced here

$$P(t) \geq P^*(t) \geq P(t)e^{-\int_0^t P(\tau)g(t-\tau)\mathrm{d}\tau} \tag{13}$$

with

$$g(\tau) = \begin{cases} 1 & 0 \leq \tau \leq t_D \\ 0 & \tau > t_D \end{cases}$$

which we quoted as relating the true photon detection probability density $P(t)$ with the effective probability density $P^*(t)$ for a TCSPC configuration with dead time t_D. The first inequality $P(t) \geq P^*(t)$ is trivial; the effect of "dead time" can only be to decrease the effective probability density $P^*(t)$ in comparison to the true density. We derive the second inequality.

First, let $P_d(t')$ be defined as follows: it is the probability that, at time t', no photon has yet been detected whose associated "dead time" overlaps with the time t. From this definition, it is clear that

$$P_d(t - t_D) = 1$$

and

$$P^*(t) = P(t)P_d(t)$$

During the time $t - t_D < t' < t$, we may argue that $P_d(t')$ obeys the following differential inequality:

$$0 \geq \frac{\mathrm{d}P_d}{\mathrm{d}t'} \geq -P(t')P_d(t') \tag{14}$$

The first inequality is trivial; P_d can only decrease as more photons have the chance to be detected. To unterstand the second, we argue as follows. Supposing we know the probability $P_d(t')$ that no photon with dead time overlap has been detected by time t', we may write the probability $P_d(t' + \Delta t')$ as

$$P_d(t + \Delta t') = P_d(t')(1 - P^*(t')\Delta t') \tag{15}$$

There is, in other words, an approximate probability $P^*(t')\Delta t'$ that a photon is *detected* during the window $(t', t' + \Delta t')$, and, given that $t' > t - t_D$, we know that this photon's dead time will overlap with time t. The use of $P^*(t')$ is crucial - a photon which arrives at the detector at t' but is not counted thanks to some previous "dead time" will not trigger a new "dead time" that interferes with detection at time t. $P_d(t' + \Delta t')$ is then approximately equal to $P_d(t')(1 - P^*(t')\Delta t)$. Solving the resulting differential equation is difficult, thanks to the $P^*(t)$ dependence. However, using the bound $P^*(t) \leq P(t)$, we may bound the change in $P_d(t')$ as follows:

$$P_d(t' + \Delta t') \geq P_d(t')(1 - P(t')\Delta t') \tag{16}$$

A trivial rearrangement, followed by taking $\Delta t \to \mathrm{d}t$, then gives the quoted differential inequality.

The differential equation obtained by setting

$$\frac{\mathrm{d}P_d}{\mathrm{d}t} = -P(t')P_d(t')$$

plus the initial condition established above, has a trivial solution:

$$P_d(t') = e^{-\int_{t-t_D}^{t'} P(\tau)\mathrm{d}\tau}$$

Rewriting this using the function g given above,

$$P_d(t) = e^{-\int_0^t g(t-\tau)P(\tau)\mathrm{d}\tau}$$

We then have the following inequality for $P_d(t)$:

$$1 \geq P_d(t) \geq e^{-\int_0^t g(t-\tau)P(\tau)\mathrm{d}\tau}$$

Since $P^*(t) = P(t)P_d(t)$, we obtain the quoted inequality

$$P(t) \geq P^*(t) \geq P(t)e^{-\int_0^t g(t-\tau)P(\tau)\mathrm{d}\tau} \tag{17}$$

as claimed. We remark that the exact behavior of $P^*(t)$ is of secondary interest to us, and that we are mostly concerned with finding the conditions under which $P^*(t) \approx P(t)$; it is for this reason that we content ourselves with this bound.

8.2 Derivation of $n^{-\frac{1}{2}}$ scaling for a 1D isotropic random walker

We present a simple derivation adapted from one given in Ref [31]. For $2k$ an even number, it is trivial to write the probability that a 1D isotropic random walker, initially at the origin, returns there after exactly $2k$ hops:

$$P(2k) = \left(\frac{1}{2}\right)^{2k} \binom{2k}{k} \tag{18}$$

To see how this is asymptotically proportional to $\frac{1}{\sqrt{k}}$, we consider Stirling's formula:

$$m! \sim \sqrt{2\pi n}\left(\frac{n}{e}\right)^n \tag{19}$$

where the $\sim$ denotes that the two quantities are asymptotic to each other. It follows that

$$\left(\frac{1}{2}\right)^{2k} \binom{2k}{k} = 2^{-2k}\frac{(2k)!}{(k!)^2} = 2^{-2k}\left(\sqrt{4\pi k}\ (2k)^{2k}\ e^{-2k}\right)\frac{1}{\left(\sqrt{2\pi k}\ k^k\ e^{-k}\right)^2}$$

$$= 2^{-2k}\frac{\sqrt{4\pi k}\ 2^{2k}\ k^{2k}e^{-2k}}{2\pi k\ k^{2k}\ e^{-2k}} = \sqrt{\frac{1}{\pi}}\frac{1}{\sqrt{k}} = \sqrt{\frac{2}{\pi}}\frac{1}{\sqrt{2k}} \propto \frac{1}{\sqrt{2k}}$$

and the $\frac{1}{\sqrt{n}}$ scaling is established.

8.3 Derivation of the power series form for $P_i(t)$

Recall from the manipulations given above that

$$P_i(t) = \sum_{k=0}^{\infty} G_k H_i^k(t) \tag{20}$$

where

$$G_k = \begin{cases} 0 & k \text{ odd} \\ 2^{-k}\binom{k}{\frac{k}{2}} & k \text{ even} \end{cases} \tag{21}$$

and

$$H_i^k(t) = \left(\frac{t}{\tau_i}\right)^k \frac{1}{k!} e^{-\frac{t}{\tau_i}} \tag{22}$$

Now, given the above definition of G_k, we may rewrite $P_i(t)$ as follows:

$$P_i(t) = \sum_{k=0}^{\infty} G_{2k} H_i^{2k}(t)$$

or

$$\begin{aligned} P_i(t) &= \sum_{k=0}^{\infty} (2)^{-2k} \binom{2k}{k} \left(\frac{t}{\tau_i}\right)^{2k} \frac{1}{(2k)!} e^{-\frac{t}{\tau_i}} \\ &= \sum_{k=0}^{\infty} (2)^{-2k} \frac{1}{(k!)^2} \left(\frac{t}{\tau_i}\right)^{2k} e^{-\frac{t}{\tau_i}} \end{aligned} \tag{23}$$

We note that the series above is not yet a power series in $\frac{t}{\tau_i}$, since the k-th term of the above contains infinitely many different powers of $\frac{t}{\tau_i}$ by virtue of $e^{-\frac{t}{\tau_i}}$. We rearrange it after proving a simple lemma.

Lemma: Suppose that, $\forall i \in \mathbb{N}$, $\sum_{j=1}^{\infty} b_{i,j}$ *is absolutely convergent to* a_i*, with* $\sum_{j=1}^{\infty} |b_{i,j}| = s_i$*. Suppose that* $\sum_{i=1}^{\infty} s_i$ *converges to* S*, such that* $\sum_{i=1}^{\infty} a_i$ *is absolutely convergent to* A*. Then, where* $f : \mathbb{N} \to \mathbb{N} \times \mathbb{N}$ *is an arbitrary bijection,*

$$\sum_{k=1}^{\infty} b_{f(k)}$$

is absolutely convergent and converges to A*.*

We first show that the quoted series is absolutely convergent. Consider

$$\sum_{k=1}^{M} |b_{f(k)}| \tag{24}$$

Let I be the largest index i appearing in the set $f(\{1, 2, \ldots M\})$, and J be the largest index J. It follows that

$$\sum_{k=1}^{M} |b_{f(k)}| \leq \sum_{i=1}^{I} \sum_{j=1}^{J} |b_{i,j}|$$

since all of the terms on the right-hand side are positive, and since the left-hand terms are a subset of the right-hand ones (which requires the injectivity of f). We know, however, that for all i and J,

$$\sum_{j=1}^{J} |b_{i,j}| \leq s_i$$

by the absolute convergence of $\sum b_{i,j}$. Then

$$\sum_{k=1}^{M} |b_{f(k)}| \leq \sum_{i=1}^{I} s_i$$

Likewise, however, for all I, we know that

$$\sum_{i=1}^{I} s_i \leq S$$

by the convergence of these terms. Accordingly, we have for all M that

$$\sum_{k=1}^{M} |b_{f(k)}| \leq S$$

so that $\sum_{k=1}^{\infty} b_{f(k)}$ is indeed absolutely convergent.

To show convergence to A, we demonstrate that for every $\epsilon > 0$ there is a finite subset $G \subset \mathbb{N} \times \mathbb{N}$ such that, given any finite set $K \supset G$,

$$|A - \sum_{(i,j) \in K} b_{i,j}| < \epsilon \tag{25}$$

To find such a G, define $I \in \mathbb{N}$ such that

1. $|A - \sum_{i=1}^{I} a_i| < \frac{\epsilon}{5}$ (using the convergence of a_i)
2. $\sum_{i=I+1}^{\infty} s_i < \frac{\epsilon}{5}$ (using the (absolute) convergence of s_i)

Given this I, choose a J such that $\forall i \leq I$,

1. $|a_i - \sum_{j=1}^{J} b_{i,j}| < \frac{\epsilon}{5I}$ (using the convergence of $b_{i,j}$)
2. $\sum_{j=J+1}^{\infty} |b_{i,j}| < \frac{\epsilon}{5I}$ (using the absolute convergence of $b_{i,j}$)

Now, define $G = \{1, 2, \dots I\} \times \{1, 2, \dots J\}$. We write

$$\begin{aligned}
\left| A - \sum_{(i,j)\in K} b_{i,j} \right| &= \left| A - \sum_{(i,j)\in G} b_{i,j} - \sum_{(i,j)\in K\setminus G} b_{i,j} \right| \\
&= \left| A - \sum_{i=1}^{I}\sum_{j=1}^{J} b_{i,j} - \sum_{(i,j)\in K\setminus G} b_{i,j} \right| \\
&= \left| \left(A - \sum_{i=1}^{I} a_i \right) + \left(\sum_{i=1}^{I} \left[a_i - \sum_{j=1}^{J} b_{i,j} \right] \right) - \sum_{(i,j)\in K\setminus G} b_{i,j} \right| \\
&\leq \left| \left(A - \sum_{i=1}^{I} a_i \right) \right| + \sum_{i=1}^{I} \left| a_i - \sum_{j=1}^{J} b_{i,j} \right| + \sum_{i=1}^{I} \left| \sum_{(i,j)\in K\setminus G} b_{i,j} \right| + \sum_{i=I+1}^{\infty} \left| \sum_{(i,j)\in K\setminus G} b_{i,j} \right|
\end{aligned}$$

By our choices, we know that the first term is bounded by $\frac{\epsilon}{5}$, and the second term is bounded by $I\frac{\epsilon}{5I} = \frac{\epsilon}{5}$. We examine the third

$$\sum_{i=1}^{I} \left| \sum_{(i,j)\in K\setminus G} b_{i,j} \right| \leq \sum_{i=1}^{I} \sum_{(i,j)\in K\setminus G} |b_{i,j}| \leq \sum_{i=1}^{I} \sum_{j=J+1}^{\infty} |b_{i,J}| \leq \sum_{i=1}^{I} \frac{\epsilon}{5I} = \frac{\epsilon}{5}$$

so that the third term is likewise bounded. For the last term,

$$\sum_{i=I+1}^{\infty} \left| \sum_{(i,j)\in K\setminus G} b_{i,j} \right| \leq \sum_{i=I+1}^{\infty} \sum_{(i,j)\in K\setminus G} |b_{i,j}| \leq \sum_{i=I+1}^{\infty} \sum_{j=1}^{\infty} |b_{i,j}| = \sum_{i=I+1}^{\infty} s_i \leq \frac{\epsilon}{5}$$

by our choice of I. Then we ultimately have

$$\left| A - \sum_{(i,j)\in K} b_{i,j} \right| \leq \frac{\epsilon}{5} + \frac{\epsilon}{5} + \frac{\epsilon}{5} + \frac{\epsilon}{5} = \frac{4\epsilon}{5} < \epsilon \tag{26}$$

such that G is as desired. Then the sum $\sum_{k=1}^{\infty} b_{f(k)}$ indeed converges to A, as desired. $\square$

With this lemma proven, we return to our series representation:

$$P_i(t) = \sum_{k=0}^{\infty} (2)^{-2k} \frac{1}{(k!)^2} \left(\frac{t}{\tau_i}\right)^{2k} e^{-\frac{t}{\tau_i}} \tag{27}$$

Given that

$$e^{-\frac{t}{\tau_i}} = \sum_{j=0}^{\infty} \left(\frac{-t}{\tau_i}\right)^{j} \frac{1}{j!} \tag{28}$$

we may regard the above series as a case of the lemma just proven, where

$$a_k = 2^{-2k} \frac{1}{(k!)^2} \left(\frac{t}{\tau_i}\right)^{2k} e^{-\frac{t}{\tau_i}} \tag{29}$$

$$b_{k,j} = 2^{-2k} \frac{1}{(k!)^2} \left(\frac{t}{\tau_i}\right)^{2k} \frac{1}{j!} \left(\frac{-t}{\tau_i}\right)^{j} \tag{30}$$

$$s_k = 2^{-2k} \frac{1}{(k!)^2} \left(\frac{t}{\tau_i}\right)^{2k} e^{\frac{t}{\tau_i}} \tag{31}$$

and all the required convergence properties are straightforward to verify (e.g. by the ratio test). We are then free to rearrange the series at will, and in particular to group the powers of $\frac{t}{\tau_i}$ together.

Consider, then, that the terms of the sum containing the factor $\frac{t}{\tau_i}$ to the power m will be precisely those terms $b_{k,j}$ for which $2k + j = m$. Then, setting $j = m - 2k$ and summing over k, we have that the coefficient of $\left(\frac{t}{\tau}\right)^m$ will be

$$\sum_{k=0}^{\lfloor \frac{m}{2} \rfloor} (2)^{-2k} \frac{1}{(k!)^2} \frac{1}{(m-2k)!} (-1)^{m-2k}$$

or

$$(-1)^m \sum_{k=0}^{\lfloor \frac{m}{2} \rfloor} (2)^{-2k} \frac{1}{(k!)^2 (m-2k)!} \tag{32}$$

Accordingly,

$$P_i(t) = \sum_{m=0}^{\infty} C_m \left(\frac{t}{\tau_i}\right)^m \tag{33}$$

with

$$C_m = (-1)^m \sum_{k=0}^{\lfloor \frac{m}{2} \rfloor} \frac{1}{2^{2k}} \frac{1}{(m-2k)!(k!)^2} \tag{34}$$

as claimed. The first few values of C_m are $C_0 = 1$, $C_1 = -1$, $C_2 = \frac{3}{4}$, $C_3 = \frac{-5}{12}$.

References

[1] William Shockley and Hans J Queisser. Detailed balance limit of efficiency of p-n junction solar cells. *Journal of applied physics*, 32(3):510–519, 1961.

[2] Bp statistical review of world energy 2019. Technical report, BP P.L.C, 2019.

[3] MC Hanna and AJ Nozik. Solar conversion efficiency of photovoltaic and photoelectrolysis cells with carrier multiplication absorbers. *Journal of Applied Physics*, 100(7):074510, 2006.

[4] Vygintas Jankus, Edward W. Snedden, Daniel W. Bright, Erhan Arac, DeChang Dai, and Andrew P. Monkman. Competition between polaron pair formation and singlet fission observed in amorphous rubrene films. *Phys. Rev. B*, 87(22):224202, Jun 2013.

[5] Lin Ma, Keke Zhang, Christian Kloc, Handong Sun, Maria E. Michel-Beyerle, and Gagik G. Gurzadyan. Singlet fission in rubrene single crystal: direct observation by femtosecond pump-probe spectroscopy. *Phys. Chem. Chem. Phys.*, 14(23):8307–8312, 2012.

[6] Aleksandr Ryasnyanskiy and Ivan Biaggio. Triplet exciton dynamics in rubrene single crystals. *Phys. Rev. B*, 84:193203, Nov 2011.

[7] Eric A. Wolf, Drew M. Finton, Vincent Zoutenbier, and Ivan Biaggio. Quantum beats of a multiexciton state in rubrene single crystals. *Applied Physics Letters*, 112(8):083301, 2018.

[8] Hikmat Najafov, Ivan Biaggio, Vitaly Podzorov, Matthew F. Calhoun, and Michael E. Gershenson. Primary photoexcitations and the origin of the photocurrent in rubrene single crystals. *Phys. Rev. Lett.*, 96(5):056604, 2006.

[9] Brantley A. West, Jordan M. Womick, L. E. McNeil, Ke Jie Tan, and Andrew M. Moran. Ultrafast dynamics of frenkel excitons in tetracene and rubrene single crystals. *The Journal of Physical Chemistry C*, 114(23):10580–10591, 2010.

[10] M Chabr, UP Wild, J Fünfschilling, and I Zschokke-Gränacher. Quantum beats of prompt fluorescence in tetracene crystals. *Chemical Physics*, 57(3):425–430, 1981.

[11] Drew M. Finton, Eric A. Wolf, Vincent S. Zoutenbier, Kebra A. Ward, and Ivan Biaggio. Routes to singlet exciton fission in rubrene crystals and amorphous films. *AIP Advances*, 9(9):095027, 2019/10/16 2019.

[12] Chaw Keong Yong, Andrew J. Musser, Sam L. Bayliss, Steven Lukman, Hiroyuki Tamura, Olga Bubnova, Rawad K. Hallani, Aurélie Meneau, Roland Resel, Munetaka Maruyama, Shu Hotta, Laura M. Herz, David Beljonne, John E. Anthony, Jenny Clark, and Henning Sirringhaus. The entangled triplet pair state in acene and heteroacene materials. *Nature Communications*, 8:15953 EP –, 07 2017.

[13] R. G. Kepler, J. C. Caris, P. Avakian, and E. Abramson. *Phys. Rev. Lett.*, 10:400, 1963.

[14] Pavel Irkhin, Aleksandr Ryasnyanskiy, Marlus Koehler, and Ivan Biaggio. Absorption and photoluminescence spectroscopy of rubrene single crystals. *Phys. Rev. B*, 86:085143, Aug 2012.

[15] WG Herkstroeter and PB Merkel. The triplet state energies of rubrene and diphenylisobenzofuran. *Journal of Photochemistry*, 16(4):331–341, 1981.

[16] Ivan Biaggio and Pavel Irkhin. Extremely efficient exciton fission and fusion and its dominant contribution to the photoluminescence yield in rubrene single crystals. *Applied Physics Letters*, 103(26):263301, 2013.

[17] Pavel Irkhin and Ivan Biaggio. Direct imaging of anisotropic exciton diffusion and triplet diffusion length in rubrene single crystals. *Phys. Rev. Lett.*, 107:017402, Jul 2011.

[18] Xionghui Zeng, Deqiang Zhang, Lian Duan, Liduo Wang, Guifang Dong, and Yong Qiu. Morphology and fluorescence spectra of rubrene single crystals grown by physical vapor transport. *Applied Surface Science*, 253(14):6047 – 6051, 2007.

[19] Yuanzhen Chen, Bumsu Lee, Danni Fu, and Vitaly Podzorov. The origin of a 650 nm photoluminescence band in rubrene. *Advanced Materials*, 23(45):5370–5375, 2011.

[20] Oleg Mitrofanov, David V. Lang, Christian Kloc, J. Magnus Wikberg, Theo Siegrist, Woo-Young So, M. A. Sergent, and Arthur P. Ramirez. Oxygen-related band gap state in single crystal rubrene. *Phys. Rev. Lett.*, 97(16):166601, 2006.

[21] Daniel D. T. Mastrogiovanni, Jeff Mayer, Alan S. Wan, Aleksey Vishnyakov, Alexander V. Neimark, Vitaly Podzorov, Leonard C. Feldman, and Eric Garfunkel. Oxygen incorporation in rubrene single crystals. *Scientific Reports*, 4:04753, 05 2014.

[22] R.A Laudise, Ch Kloc, P.G Simpkins, and T Siegrist. Physical vapor growth of organic semiconductors. *Journal of Crystal Growth*, 187(3–4):449 – 454, 1998.

[23] S. Cova, M. Ghioni, A. Lotito, I. Rech, and F. Zappa. Evolution and prospects for single-photon avalanche diodes and quenching circuits. *Journal of Modern Optics*, 51(9-10):1267–1288, 2004.

[24] Desmond O'Connor. *Time-correlated single photon counting*. Academic Press, 2012.

[25] M. Chabr, U.P. Wild, J. Funfschilling, and I. Zschokke-Granacher. Quantum beats of prompt fluorescence in tetracene crystals. *Chemical Physics*, 57(3):425–430, 1981.

[26] Jonathan J Burdett, Geoffrey B Piland, and Christopher J Bardeen. Magnetic field effects and the role of spin states in singlet fission. *Chemical Physics Letters*, 585:1–10, 2013.

[27] Hiroyuki Tamura, Miquel Huix-Rotllant, Irene Burghardt, Yoann Olivier, and David Beljonne. First-principles quantum dynamics of singlet fission: Coherent versus thermally activated mechanisms governed by molecular π stacking. *Phys. Rev. Lett.*, 115:107401, Aug 2015.

[28] Sidney Redner. *A Guide to First-Passage Processes*. Cambridge University Press, 2001.

[29] Wolfgang Pfluegl and Robert J. Silbey. Long-time properties of random walks with a single trap. *Phys. Rev. E*, 58:4128–4133, Oct 1998.

[30] Demétrio A da Silva Filho, E-G Kim, and J-L Brédas. Transport properties in the rubrene crystal: electronic coupling and vibrational reorganization energy. *Advanced Materials*, 17(8):1072–1076, 2005.

[31] Gregory Lawler. *Random Walk and the Heat Equation*. American Mathematical Society, Providence, RI, 2010.